A Study on the Evaporation and Dynamic Wicking in a Passive Air Freshener

by

Jing Yuan

A Dissertation Presented in Partial Fulfilment
Of the Requirements for the Degree
Doctor of Philosophy

Approved October 2021 by the
Graduate Supervisory Committee:

Kangping Chen, Chair
Marcus Herrmann
Huei-ping Huang
Liping Wang
Yang Jiao

ARIZONA STATE UNIVERSITY

December 2021

ABSTRACT

In this dissertation, two types of passive air freshener products from Henkel, the wick-based air freshener and gel-based air freshener, were studied for their wicking mechanisms and evaporation performances.

The fibrous pad of the wick-based air freshener is a porous medium that absorbs fragrance by capillary force and releases the fragrance into the ambient air. To investigate the wicking process, a two-dimensional multiphase flow numerical model using COMSOL Multiphysics was built. Saturation and liquid pressure inside the pad were solved. Comparison between the simulation results and experiments shows that evaporation occurs simultaneously with the wicking process. The evaporation performance on the surface of the wicking pad was analyzed based on the kinetic theory, from which the mass flow rate of molecules passing the interface of each pore of the porous medium is obtained. A 3D model coupling the evaporation model and dynamic wicking on the evaporation pad was built to simulate the entire performance of the air freshener to the environment for a long period of time. Diffusion and natural convection effects were included in the simulation. The simulation results match well with the experiments for both the air fresheners placed in a chamber and in the absent of a chamber, the latter of which is subject to indoor airflow.

The gel-based air freshener was constructed as a porous medium in which the solid network of particles spans the volume of the fragrance liquid. To predict the evaporation performance of the gel, two approaches were tested for gel samples in hemispheric shape. The first approach was the sessile drop model commonly used for the drying process of a pure liquid droplet. It can be used to estimate the weight loss rate and time duration of the

evaporation. Another approach was to simulate the concentration profile outside the gel and estimate the evaporation rate from the surface of the gel using the kinetic theory. The evaporation area was updated based on the change of pore size. A 3D simulation using the same analysis was further applied to the cylindrical gel sample. The simulation results match the experimental data well.

ACKNOWLEDGMENTS

My graduate study at Arizona State University is one of the unforgettable experiences in my life. I would like to sincerely thank my advisor, Prof. Kangping Chen for guiding, supporting, and being patient with me over the years. Prof. Chen provided me the opportunity to work on this project and a tremendous help to finish the project. It was a great fortune being his student since he set a perfect example as a dedicated researcher, responsible instructor, and lifelong learner. His dedication to research and unsparing support always motivated me to deepen my knowledge and improve my skills in this area.

I gratefully acknowledge Henkel for their financial support. It has been a great experience working with the project leader Debra Park and Kevin Hafer. This project would not have been perfectly done without their guidance and feedback. Many thanks to Kevin for sharing the experiment results with me. I would also like to acknowledge the committee members Dr. Marcus Herrmann, Dr. Huei-ping Huang, Dr. Liping Wang, and Dr. Yang Jiao for their advice and help on my research. Additionally, I would like to thank my academic advisor Amy Newberg for all her help through these years.

Also, I would like to thank my lab-mates Dr. Shen and Dr. Huang, my friend Pengwu Yan and Greg Vetaw for their professional help and kindest patience. I appreciated your timely help every time. To my valuable friends, Samantha, Guangqi, and Eric who always took care of me and stood by me during the highs and lows I have had. You helped me go through the days I doubt myself. Your company and encouragement always relieved my stress and kept me sane. Your enthusiasm for work and life lights up my world and always kept me motivated. Thank you for putting up with me.

Lastly and most importantly, my deepest gratitude goes to my families for their unconditional love and support. I would like to thank my father, mother, my cousin, my dearest lovely grandma, who has always been the pillar of my strength throughout my life. This work would not have been possibly done without them. Talking to my families has always been a source of happiness and inspiration. You are always my greatest treasure and pride. I miss you so much.

TABLE OF CONTENTS

Page

CHAPTER Page

LIST OF TABLES

LIST OF FIGURES

Figure Page

Figure Page

CHAPTER 1

INTRODUCTION

Capillary transport in porous materials has attracted considerable interest in various modern applications in science, industry, and daily life. For example, in biomedical applications, membrane-based lateral flow tests are used in biomedical diagnostics to provide a quick and low-cost detection for microfluidic systems [1] [2]. In recent years, the interest in the medical utility of microfluidic paper-based analytical devices where wicking makes passive transport of fluids without active pumping practical has turned to the development of two-dimensional lateral flow assays and three-dimensional microfluidics [3] [4]. Fries et al. [5] introduced an application for metallic porous material used in propellant management devices, which are designed to ensure gas free delivery of propellant during the acceleration of the flight. Wicking materials are also used in heat pipes and vapor chambers when managing thermal control for compact electronic systems in various fields [6]. The development of nanostructured thin film wicks in the past decades creates opportunities for high-performance vapor chambers with largely reduced package resistance [7]. Besides these applications, wicking materials are also used for fragrance dispersion units in consumer products. Passive air fresheners are becoming more popular in recent years for their zero cost of extra energy and artistic housing design. One type of passive air freshener is comprised of a bottle filled with a liquid fragrance and a diffuser pad made of hydrophilic microfiber as shown in Figure 1. The leg of the pad is inserted into the bottle and draws the liquid fragrance from the bottle up to the pad against gravity via capillary force. The exposure of the liquid-wetted pad to ambient air causes the

fragrance to evaporate. The fragrance vapor then disperses to the room via advection and diffusion. This process is similar to plants transporting water to the leaves from their roots via xylem through transpiration, which is an evaporation process that occurs at the leaves. Based on an article published in 2017, the global market for air fresheners exceeds US $10 billion annually and is increasing in most countries. In a European population survey, passive air fresheners are used by 30% of the surveyed population at least once a week in homes and by 89% at least once a month in homes [8].

Fig.1 An air freshener product of GLADE® EXPRESSIONS™ oil diffuser comprised of a bottle of liquid fragrance and a wicking pad.

From a product development point of view, the performance of such a passive air freshener can be measured in terms of the speed as well as the duration of the evaporative process for a given amount of liquid fragrance stored in the bottle. Accurate prediction of the evaporation rate and the time it takes to empty the bottle is essential for the sizing of the bottle and the pad, which in term can affect the aesthetic element of the design. The study reported in this thesis intends to lay the groundwork for developing such a predictive

tool. Several elements important for building this predictive model must be first explored and studied.

1.1 Capillary transport

Due to the widespread applications, many theoretical models have been developed for capillary transport. Wicking is the term used to describe the phenomenon that occurs when dry porous material is put into contact with a liquid. The porous material will absorb liquid due to capillary force (i.e. capillary rise). Many studies on porous media assume that the pore space can be modeled by a bundle of capillary tubes, which is perhaps the simplest porous medium model. Such a model was first presented by Lucas and Washburn, respectively [9] [10]. The capillary flow in a porous medium is governed by a momentum balance among the inertial, capillary, viscous frictional force, as well as the hydrostatic pressure:

$$-\rho\frac{d\left(h\dot{h}\right)}{dt}=-\frac{2\sigma\cos\theta}{R_s}+\frac{8\mu}{R_d^2}h\dot{h}+\rho_f gh, \tag{1.1.1}$$

where σ is the vapor-liquid surface tension, θ is the contact angle formed between the solid and the liquid, R_s is the mean static radius (or "capillary pressure effective radius"), which can be calculated from the maximum obtainable height measured from experiments [11]. h is the capillary rise. ρ_f and g are the density of the fluid and gravitational acceleration, respectively. μ is the dynamic viscosity of the fluid, R_d is the mean hydrodynamic radius of the capillary pores, which is different from the static radius as it depends also on the tortuosity of the pores [12]. The first term on the right-hand side represents the capillary pressure generated by the liquid-vapor interface, which is obtained

through the Young-Laplace equation [13]. Hagen-Poiseuille Law is applied to the viscous frictional force, which results in the second term on the right-hand side [14]. A more widely used Lucas-Washburn (L-W) equation neglects the inertia term and gravity term in the momentum balance equation (1.1.1) and it results in a simple relationship between the capillary rise height and time in a bundle of aligned capillary tubes:

$$h(t)=\sqrt{\frac{R_e\sigma\cos\theta}{2\mu}t}, \tag{1.1.2}$$

where R_e, the effective pore radius, is obtained through $R_e=\frac{R_d^2}{R_s}$ [15]. The L-W model assumes the capillary tubes are aligned with the flow direction, which is a one-dimensional model. The L-W model predicts that the meniscus height is proportional to the square root of time, $h\sim t^{1/2}$. A large number of experimental results agree well with the predicted capillary rise from the L-W model [14] [16]. However, the validity of the L-W model is limited since it predicts infinite velocity at the initial stage. Improvements to the L-W model have been made over the years. Many researchers have also tried to add the neglected terms to the momentum balance in the L-W model to extend the validity of the derived solutions for different applications [11] [16-22]. These include the inertia force of the liquid mass inside the tube [11] [16-19]; the pressure loss at the tube entrance [17] [18]; and the dynamic contact angle [19] [20]. Levine et al. [21] examined the momentum balance for the sink flow from the reservoir towards the tube entrance and investigated the departure from Poiseuille flow in the vicinity of an advancing meniscus in a vertical cylindrical capillary. A detailed mathematical theory for the capillary rise in tubes is presented. Zhmud et al. [22] studied the special case of capillary rise of surfactant solutions,

which includes diffusion-controlled processes at the gas-liquid interface. The relationship for capillary rise dynamics with strong depletion of the interfacial region is obtained. Stange et al. [23] used the linear momentum equation for the capillary rise of liquid between parallel plate described by Dreyer et al. [24] and applied to the circular tubes. Drop tower experiments were presented with capillary flow in a single tube under microgravity condition and compared measurements with corresponding numerical solutions. Their work shows that the capillary rise process can be divided into four successive stages with i) an initial $h \sim t^2$ domain corresponding to the acceleration of the liquid; ii) a $h \sim t$ domain dominated by the convective pressure loss in the liquid reservoir and the capillary tube, with a constant rise velocity; iii) a $h \sim \sqrt{t}$ domain related to viscous dissipation neglecting the influence of inertia and gravity; and finally a $h \sim 1 - e^{-(1+t)}$ domain due to the gravitational deceleration. The inertia-dominated flow regime in capillary tubes was also examined by Quéré [16]. It should be emphasized that all these works are limited to one-dimensional models, and they have all neglected evaporation on the surface of the porous material.

Another approach is to model the wicking of liquids into porous media using Darcy's law. In 1856, Darcy [25] reported his experiments-based formula for flow in a porous medium. Darcy proposed a simple relation between the average velocity of a liquid and the pressure gradient in a fully saturated porous medium:

$$\nabla p = -\frac{\mu}{\kappa}\vec{v}, \tag{1.1.3}$$

where p and v are the average pressure and average velocity, and κ is the permeability of

the porous medium. Darcy's law together with the continuity equation provides a mathematical model suitable for a wide variety of applications involving porous media flow, for which the pressure gradient is the major driving force. Masoodi and Pillai [15] proposed a Darcy's-law-based model coupled with the mass conservation equation accounting for matrix swelling and liquid absorption. The predicted wicking rate is compared with the experimental result and their modified Washburn equation contains the tortuosity of the porous wick [26]. Many finite-element-method-based numerical simulations of imbibition into two-dimensional porous media have been performed using Darcy's model [27]. Brinkman's model [28], which is an extension of Darcy's law that includes the dissipation of kinetic energy by viscous shear is widely used to simulate fast flow in porous media. For instance, to simulate the fluid flow in lateral flow assay in the biosensor detection field [29], and wicking in structured nanochannels [30]. Recently, Richard's model [31], which modifies Darcy's model for partially saturated porous medium has also been used in studying the wicking behavior in 2D thin fibrous materials [34-37]. Richards' model is based on the assumptions that the capillary pressure and relative permeability depend on local saturation. Ashari et al. [32] presented a study for the spreading of fluids in thin fibrous sheets with random in-plane fiber orientation by solving 2D Richards' equation. Perez-Cruz et al. [33] and Tirapu-Azpiroz et al. [34] applied Richards' model to simulate imbibition into paper-based networks respectively on different 2D geometries. In both studies, the results agree with the experimental results well.

1.2 Evaporation over the porous media surface

Fries et al. [5] and Barry et al. [35] modified the L-W model with evaporation by adding a viscous pressure loss due to the flow velocity to refill the evaporated liquid. It is assumed that the evaporation rate is constant over vertically positioned metallic weaves. The analytical result is compared with the experimental data by calculating the dimensionless number relating the maximum reachable height with gravity and evaporation to the maximum height without evaporation. The predicted capillary rise is found to be larger than the measured ones. The model of Fries et al. assumed the system to be either wet or dry. Rogacs et al. [6] applied the evaporation model of Fries et al. and neglected the inertia term to extract the wettability of nanostructured wicks based on optical imaging. The analytical solution for capillary rise is derived with the gravitational effect neglected. They concluded that for typical thin-film sample sizes and experimental conditions, the gravitational effect is negligible, but the evaporation effect plays a significant role in establishing the filling rate. Jahanshahi-Anbuhi et al. [36] extended the modified model of Rogacs et al. [6] by taking into account the effect of the water content of the paper fibers to predict the capillary rise in pullulan films while neglecting gravity. The prediction matches well with experimental data, but only for short paper strips with constant width. Liu et al. [37] applied a mathematical model based on the momentum balance including viscous resistance, capillary force, and evaporation with a constant rate to predict the capillary rise in filter diagnostic paper with different widths. The predicted capillary rise agreed well with experimental data, but the deviation is significant for wider wicks at longer times. An empirical equation (1.2.1) below, from the ASHRAE handbook [38] is

used by both Jahanshahi-Anbuhi et al. [36] and Liu et al. [37] to calculate the constant evaporation rate when water is used as the wetting fluid, which considers the environmental conditions of temperature and relative humidity:

$$\dot{m}_{evp} = \left(P_s - p\right)\left(0.089 + 0.0782 V_{air}\right) / Y, \tag{1.2.1}$$

where P_s, p, V_{air}, Y are the water saturation pressure, the partial pressure of water vapor in the air, the airflow rate, and the latent heat of vaporization of water, respectively. The predicted wicking height with evaporation rate included agreed well with the experimental data. Camplisson et al. [39] studied the wicking in two-ply channels in paper-based microfluidic devices. A new expression for capillary rise was derived using Darcy's law but including a term for evaporation. The evaporation rate is estimated from experimental measurements, and it is a constant. Beyhaghi et al. [40] proposed another approach, evaluating the evaporation rate by solving a diffusion equation for the vapor transport in the gas phase. All of the above theories assume the evaporation rate is constant over the wick and independent of time, which is estimated either from experimental measurements [5] [39] or by the empirical correlation equation (1.2.1) [36] [37]. However, in the presence of airflow in the environment or gravity, the evaporation rate is a function of the wicking height and time. Veran-Tissoires et al. [41] studied efflorescence, which refers to crystallized salt structures forming at the surface of a porous medium. They determined that evaporation during imbibition in a porous medium would result in a non-uniform evaporation flux distribution, with a higher flux within the imbibition front surface. Van Engaland et al. [42] developed a one-dimensional Darcy-based model of imbibition in porous medium including the effect of gravity and evaporation by considering the quasi-

steady diffusive and Stefan-convective transports of the vapor in the gas phase. The dynamic of the liquid-gas interface is governed by the competition between capillary imbibition, gravity drainage, and evaporation. The analytical solution for the dynamics of the liquid front is derived. The validation of their model is limited due to the restriction of one dimension along the vertical direction. To better predict the entire evaporation performance of a wicking pad, the time-varying concentration of the tracer species needs to be obtained using the convection and diffusion module combined with dynamic wicking.

1.3 Scope of the Thesis

The objective of this dissertation is to use fluid dynamics and mass transfer principles to model the entire process of the flow and evaporation of the liquid fragrance in a passive air freshener shown in Figure 1 during the wet-out of the wicking pad and after the pad is fully wetted. The project was initiated and funded by Henkel USA before their move to the east coast.

The evaporation of the fragrance from the porous pad drives a dynamic wicking process in the pad-bottle system: because of mass conservation, the pad, which is a porous material, must draw the same amount of liquid from the bottle as the amount of evaporating vapor. This is required for maintaining the height of the wetted portion of the pad for quasi-steady operation (nearly constant total evaporation rate from the entire pad). Otherwise, the effective area of evaporation will decrease due to the reduced wetted area, causing a drop in the performance of the total evaporation rate. It is this mass flow rate balance that couples the process of evaporation from the pad surface to the dynamic wicking in the pad-bottle system. Our study shall focus on the fundamental aspects of this coupled dynamics.

We use experiments, analysis, and numerical simulations to study the performance and the duration of the evaporation rate.

1.4 Organization of the Thesis

In Chapter 2, a time-dependent two-dimensional numerical model on the wicking behavior without evaporation is presented. The model uses the methodology from Tirapu-Azpiroz et al. [34] to solve for the volumetric content of the wetting phase in porous media. The result is compared to the experimental results provided by Henkel.

Chapter 3 studies the dynamic evaporation model in a single capillary tube. The evaporation rate along the surface of porous material depends on the capillary pressure and the concentration of fragrance vapor. In Chapter 4, a dynamic wicking model is built based on the passive air freshener designed by Henkel and is coupled to the surface evaporation through the interface condition. The coupled model for dynamic wicking and evaporation is solved numerically.

Chapter 5 describes the experiments performed by Henkel. The evaporation performances are recorded for the passive air freshener placed in a chamber and in a room respectively. In Chapter 6, the numerical simulations are discussed. To better compare with the experimental results, 3D models are built for the wicking unit placed in a chamber and in a room.

Chapter 7 provide preliminary studies on the performance of gel-based passive air freshener. The evaporation performances of the samples in a cylindrical shape and hemispherical shape are studied by numerical models and compared to experimental results.

In Chapter 8, we summarize the outcomes from the presented study and discuss the possible future improvements and works.

CHAPTER 2

WICKING PROCESS

2.1 Literature review on two-dimensional wicking process

Various analytical and numerical models have been developed in the past few years to investigate wicking behavior in 2D or 3D structures considering the geometry of the porous medium. Medina et al. [43] derived an analytical solution for imbibition in two-dimensional triangular and rectangular shapes of blotting paper. Mendez [1] performed a study of imbibition in nitrocellulose paper with different shapes. Numerical simulations were performed solving Darcy's law and mass balance equation neglecting gravity for imbibition into porous membranes of alternative two-dimensional shapes with a thin stem contacting the reservoir. Flow velocities at different locations on the wicking membrane were tracked mathematically and experimentally. Fu et al. [2] studied the transport in rectangular channels with a sudden width expansion. The flow in fully wetted connected segments is analogous to an electron flow in the electrical circuit. The transport time is calculated, and it is consistent with the experimental result. The electrical circuit analogous model attracted great interest in understanding the 2D wicking performance for paper-based materials, for example, tortuous linear paper network [44], assembled devices with an absorbent shunt on the paper strip [45], and a sponge shunt integrated on lateral flow assays [46].

Brinkman's form of Darcy's law accounts for momentum transport through viscous effects:

$$\nabla p = -\frac{\mu}{\kappa}\vec{v} + \mu_e \nabla^2 \vec{v}, \tag{2.1.1}$$

where μ_e is the effective viscosity. A 3D simulation for a steady-state flow using Brinkman's equation was performed by Choi et al. [29] to evaluate the phenomena of fluidic delay in lateral flow assay. Poudel et al. [30] used Brinkman's equation to predict the spreading distance of the water droplet placed on the SiO_2 surface as water wicks into nanochannels under the surface from the pores at a steep rate.

Porous materials with a wide range of pore sizes are usually unsaturated or partially saturated. Richards' equation, which couples Darcy's law and conservation of mass, provides a strategy for unsaturated porous media:

$$\frac{\partial S_w}{\partial t} = \nabla \cdot \left[K\left(S_w\right) \frac{\partial P_c}{\partial S_w} \nabla S_w \right], \tag{2.1.2}$$

where S_w is the volume fraction (also called saturation) of the wetting fluid, P_c is the capillary pressure, and

$$K\left(S_w\right) = \frac{\phi \kappa\left(S_w\right)}{\mu} \tag{2.1.3}$$

is the equivalent fluid conductivity, where ϕ is the porosity, μ is the dynamic viscosity, and κ is the permeability of the porous material. Ashari et al. [32] solved Richards' equation to simulate moisture absorbency in fibrous sheets. The capillary pressure term is the result of their Full Morphology method [47]. The relative permeability is determined using the Full Morphology-Stokes method [48]. A time-dependent two-phase flow model based on Richards' equation is used to simulate the wetting process of two-dimensional paper networks by Perez-Cruz et al. [33] and Tirapu-Azpiroz et al. [34]. The time-dependent advancement of the saturation of the wetting phase was solved. In both studies,

the capillary pressure and permeability are functions of saturation by applying the Brooks-Corey model [49], which is well known for modeling imbibition in soils. By applying Richard's equation, the diffusive saturation field throughout a porous medium can be predicted. Gravity is ignored in all the above studies.

2.2 Two-dimensional simulation on wicking performance

We employ numerical simulation to study the wicking behavior of our air freshener pad using the finite-element package COMSOL Multiphysics by coupling Darcy's law with the Phase Transport in Porous Media Interface in COMSOL. It is assumed that the liquid is transported into a completely dry finite domain along the pad. The effects of fiber swelling, inertial forces are neglected [34]. Combining Darcy's law with the continuity equation, we have

$$\frac{\partial}{\partial t}\left(\phi\rho\right)+\nabla\cdot\rho\left[-\frac{\kappa}{\mu}\left(\nabla p+\rho g\right)\right]=0. \tag{2.2.1}$$

The Phase Transport in Porous Media Interface in COMSOL uses separate equations for the volume fraction s_i of the wetting or non-wetting fluid i respectively:

$$\frac{\partial}{\partial t}\left(\phi\rho_i s_i\right)+\nabla\cdot\left(-\rho_i\kappa_s\frac{\kappa_{ri}}{\mu_i}\left(\nabla p_i+\rho_i g\right)\right)=0, \tag{2.2.2}$$

where κ_s is the intrinsic permeability for single-phase. p_i and ρ_i are the pressure and density of phase i, respectively. The relative permeability κ_{ri} for the wetting and non-wetting phases are calculated based on Brooks and Corey model [49] as below:

$$\kappa_{rs_w}=\left(s_w\right)^{3+2/\lambda}, \tag{2.2.3}$$

$$\kappa_{rs_{nw}}=s_{nw}^2\left(1-\left(1-s_{nw}\right)^{1+2/\lambda}\right), \tag{2.2.4}$$

where λ is the pore-size distribution, which has to be determined experimentally. The subscript *w* and *nw* represent the wetting phase and non-wetting phase respectively. Brooks and Corey [49] [50] reasoned that for media having a uniform pore size, the index would be a large number, media with a wide range of pore sizes should have a small value of λ. Based on Brooks and Corey model [34] [33] [49], the capillary pressure depends on both saturation and the geometry of the pore space at the interface. Based on the observation from a large number of their experimental data, they proposed

$$s_w = \left(\frac{P_{ec}}{P_c} \right)^{\lambda}, \tag{2.2.5}$$

where s_w is the effective saturation of the wetting phase, P_{ec} is the nonwetting entry capillary pressure, which describes the minimum air pressure needed to act on the liquid phase in the medium to allow the air to invade the porous medium [51]. P_c is the capillary pressure.

As shown in Figure 2, a 2D simulation domain is built based on the air freshener model used in our experiment. The wicking pad is 6cm x 10cm, with a 1cm x 4cm stem immersed into the liquid and reaching the bottom of the fragrance container. The height of the fragrance in the container is initially 2cm. It is assumed that no evaporation occurs at the surface of the pad during capillary rise and the pad is initially dry with the pores fully occupied by the air. Darcy's law is used to compute the liquid pressure. The phase transport module computes the saturation of air and the liquid. The bottom edge of the simulation domain is the entrance where the wicking pad contacts the liquid. Assume the liquid level in the container stays the same during the wicking process, as the wicking process does not

take up much liquid. The boundary condition for the bottom boundary for Darcy's law is the atmospheric pressure for the liquid phase. Dirichlet boundary condition is used for the phase transport module at the bottom boundary, where the saturation of liquid is defined using a smoothed step function from 0 to its maximum saturation 1 at the initial time step. At the top boundary, the liquid pressure is the hydrostatic atmospheric pressure minus the capillary pressure at the top [15]. The mass flux for the air phase is defined which results from the pressure gradient given in the Darcy model. It is assumed to be no flux and no flow at the side boundaries of the wicking pad and the stem.

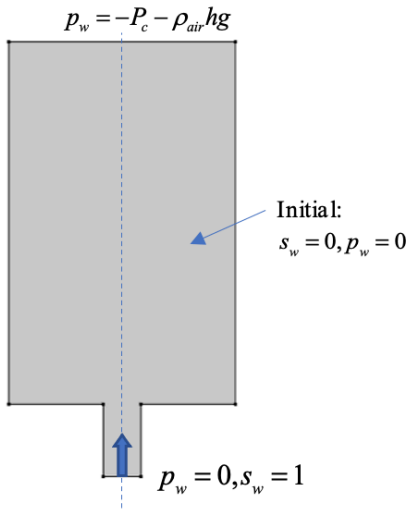

Fig. 2 The 2D simulation domain and the boundary conditions.

These equations allow us to solve for saturation and liquid pressure inside the wicking pad. A mapped mesh is generated as shown in Figure 3. The dense mesh at the bottom is needed to resolve the very steep saturation gradient in the initial phase of the process. Mesh refinement is processed by resolving the model using Darcy's law with the mesh refined 100% each time. Mass flux is tracked for each steady-state study to determine the order of

convergence. The selected mesh contains 42,721 mesh vertices. A time-dependent study is performed using the implicit time-stepping method BDF [52]. The relative tolerance for pressure is 10^{-6}. The initial time step is set to be 0.0001s since there are very steep gradients in the volume fractions of the liquid and air.

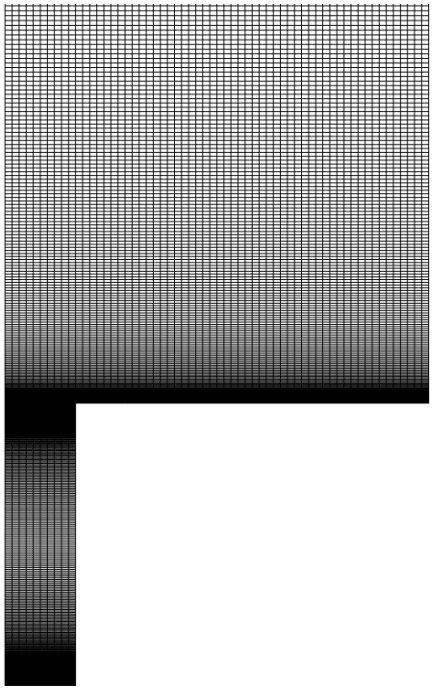

Fig. 3 Mapped mesh for the 2D simulation domain.

2.3 Materials and experiments

The main properties of the fragrance liquid are listed in Table 1 provided by Henkel.

Table 1. Properties of the Fragrance Fluid at 68°F

	ρ_f [kg/m^3]	μ [Pa.s]	σ [N/m]
Fragrance	984.6	0.0058	0.025

The wicking pad is a 1.5mm-thick multi-ply paper-like fibrous material (55pt). The properties of the wicking pad are listed in Table 2.

To determine the porosity of the porous material, immerse a piece of the sample with the same material and thickness in the fragrance liquid under vacuum for a sufficiently long time to fill all the pore space with the liquid. By weighing the sample before and after imbibition and coupling the data with the density of the liquid, the pore volume can be obtained. The porosity is the fraction of the bulk volume that is occupied by pore space.

Table 2. Properties of the Wicking Pad

Material	size [cm]	porosity	R_e [μm]	λ
55pt	10 x 6 x 0.15, 4 x 1 x 0.15	60%	8	2

To obtain the effective pore radius of the porous material and the pore-size distribution index, a separate experiment is performed by measuring the capillary performance for a 10mm-width wicking strip with the same material and thickness. The L-W equation (1.1.2) provided the relationship between the capillary rise and time. It can be modified to give the capillary mass instead of the height, resulting

$$w_{cap}^2 = \left(\phi \rho_f A_b\right)^2 \frac{\sigma \cos\theta}{2\mu} R_e t, \tag{2.3.1}$$

where w_{cap} is the weight change during wicking, A_b is the cross-sectional area of the strip sample. The weight-measurement approach is performed to overcome the difficulties when the liquid front is hard to measure precisely. The top of the wicking strip is hung by a holder. By recording the weight change of the liquid every 20 seconds, the liquid mass absorbed by the wicking strip at a different time can be obtained. Since a short wicking strip is used in the experiment, the evaporation effect and gravity effect are negligible. The

experimental result shows a good $h \sim \sqrt{t}$ relationship for the first 100s, which is consistent with the Lucas-Washburn equation. $R_e \cos\theta$ is found to be 4μm by fitting the experimental data for the first 100s to the equation (2.3.1). Figure 4 shows the comparison of experimental data and the computed results of mass change during wicking using (2.3.1). The contact angle of the fragrance liquid is assumed to be constant at 60° [53]. Thus, the effective pore radius is 4μm. The intrinsic permeability of the porous material is derived by [5] [15]:

$$\kappa_s = \frac{\phi R_e^2}{8}. \tag{2.3.2}$$

Lu et al. [51] examined the gap between entry pressure and mean capillary pressure with a wide range of the mean radius of the porous medium. The mean capillary pressure is calculated by the Young-Laplace equation $\frac{2\sigma\cos\theta}{R_e}$. It is observed that the difference between the entry pressure and the mean capillary pressure is negligible. In our study, the entry capillary pressure is set to be the mean capillary pressure for simplicity. Corey [50] claims that the pore-size distribution index is about 2 for typical porous media. Figure 4 shows a good agreement with the experimental result when applying the parameters mentioned above to the two-dimensional simulation model.

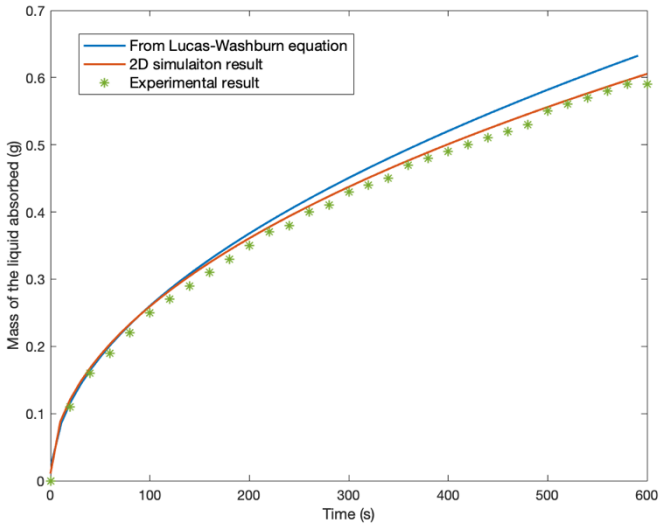

Fig. 4 The liquid mass absorbed by the wicking strip as a function of time with experimental data compared with results of the L-W model and 2D simulation.

The experiments testing the two-dimensional wicking performance were performed with the air freshener unit placed in a chamber with dimensions of $37\text{cm} \times 35\text{cm} \times 46\text{cm}$ under room temperature 68°F. There's no noticeable airflow around the wicking unit. The weight of the liquid left in the bottle is measured every 100 seconds, Figure 5 shows some of the wicking conditions recorded.

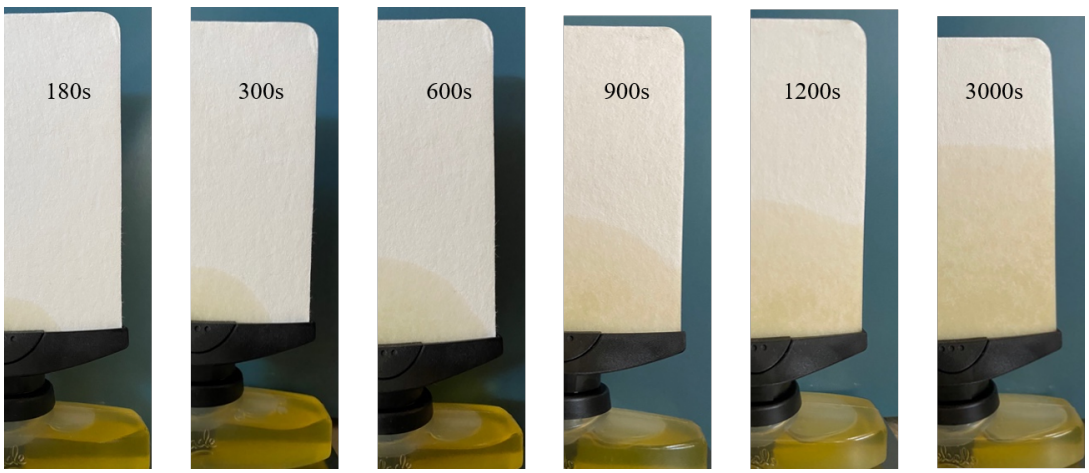

Fig.5 Wicking performance from experimental results.

2.4 Simulation results compared with experimental results

Figure 6 shows the two-dimensional simulation results plotting the volume fraction of the liquid inside the wick at t=50s, 150s, 400s, 600s, and 900s.

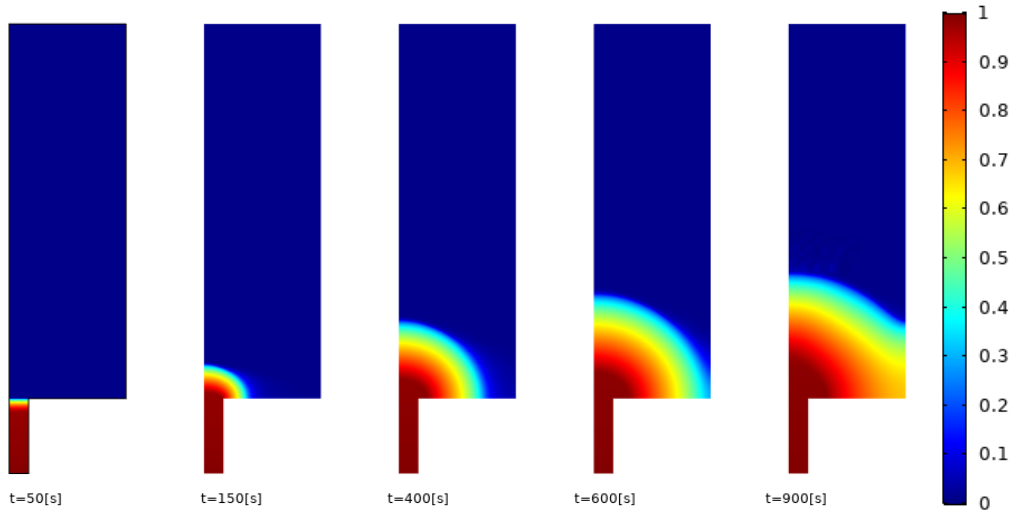

Fig.6 The liquid saturation profile in the wicking pad at t=50s, 150s, 400s, 600s, and 900s from simulation results.

The simulation results for the first 1200s agree well with the experimental results. It is also observed from the simulation that the increment of the wetting area or speed of the liquid front is approximately constant after the transition. The level of the liquid becomes approximately even after 1200s (i.e. the phase front becomes horizontal). The mass of the liquid absorbed during the wicking process from the simulation and experiment are plotted in Figure 7.

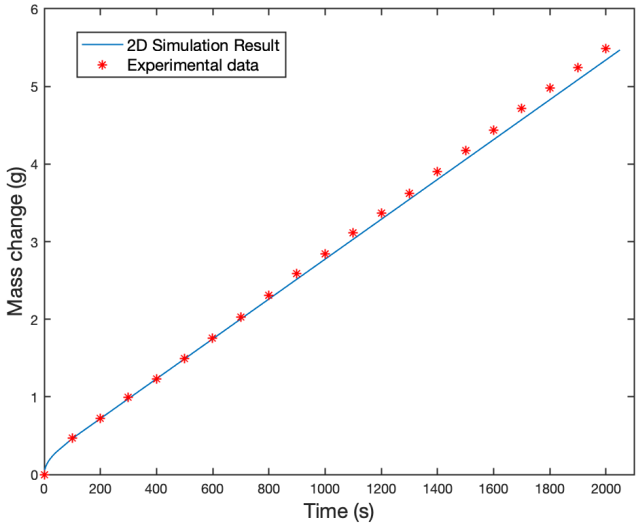

Fig. 7 The comparison of the 2D simulation result with experimental result on the growth of the capillary weight

Figure 7 shows that the measured mass change is greater than the predicted wicking rate by the simulation after around 1200s. The experiment shows that it takes 1 hour and 28 minutes to get the pad fully soaked, and a total weight loss of 40mg was observed during the entire process. The liquid front rises evenly in the pad for approximately 70% of the total wicking period. The liquid rises much slower as the liquid front reaching the top of the pad. These imply that evaporation from the pad surface occurs simultaneously with the wicking process even though no airflow is present. Evaporation will be considered in the next chapter.

CHAPTER 3

EVAPORATION MODEL

As discussed in Chapter 1, the evaporation effect has been explored by many researchers when analyzing wicking. However, most of them have assumed that the evaporation rate is constant both spatially and temporally. In this chapter, we will first review the equilibrium evaporation model. A new dynamic evaporation model is developed for a single capillary tube. The evaporation model can be coupled with the dynamic wicking model to predict the evaporation performance both for the wicking process and when the wick is fully wet.

3.1 The equilibrium theory

In the simplest model, the structure of the wicking pad can be modeled as thousands of tiny capillary pores. The interfacial region between two homogeneous phases, the liquid fragrance and air, contains matter in a distinct physical state. If evaporation is occurring, there must be a mass movement of gas from the phase interface. The interface between fragrance and air behaves as it is in a state of uniform tension. It is convenient to represent the interface as a geometric surface in tension. Furthermore, as the fragrance wets the wicking pad, the liquid-air interface at each pore is curved.

When an evaporating interface between a liquid and its vapor phase is curved, because of the capillary effect, the equilibrium vapor pressure, p_v, the pressure at which the liquid and its vapor phase are in equilibrium, will be different from the saturation vapor pressure, p_{sat}, which is the equilibrium vapor pressure for a flat interface. A curved meniscus shown in Figure 8 corresponds to a capillary tube with the liquid wetting the inner surface. The

equation relating the equilibrium vapor pressure p_v to the saturation vapor pressure p_{sat} at the surface temperature T is called the Kelvin equation [54]. The Kelvin equation describes the change in vapor pressure of a curved liquid-vapor interface on evaporation:

$$\ln \frac{P_v}{P_{sat}} = \frac{2H\sigma V_l}{R_u T}, \tag{3.1.1}$$

where H is the mean curvature of the meniscus, σ is the liquid-vapor surface tension, V_l is the liquid molar volume, R_u is the ideal gas constant, T is the surface temperature.

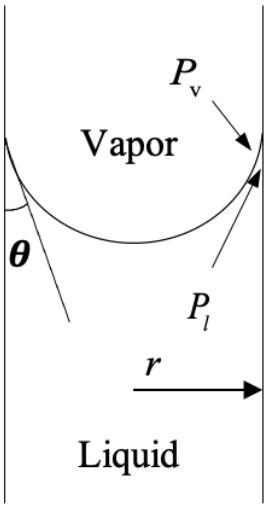

Fig.8 Curved interface: convex meniscus viewed from the liquid side.

The curvature of the meniscus is determined by the pore radius r and the contact angle of the fragrance θ. If the meniscus is a convex viewed from the liquid side as shown in Figure 8,

$$2H = -\frac{2}{r}\cos\theta, \tag{3.1.2}$$

and (3.1.1) becomes

$$\ln\frac{P_v}{P_{sat}} = -\frac{V_l}{R_u T}\frac{2\sigma}{r}\cos\theta. \tag{3.1.3}$$

Thus, the equilibrium pressure is expressed as

$$P_v = P_{sat}\exp\left(-\frac{V_l}{R_u T}\frac{2\sigma}{r}\cos\theta\right). \tag{3.1.4}$$

This equation recovers to $P_v = P_{sat}$ for a flat liquid-vapor interface, where the contact angle is 90°. Eqn. (3.1.4) shows that the vapor pressure on a liquid-wetted tube is smaller than the saturation vapor pressure, which makes it harder to evaporate the liquid.

The Kelvin effect, however, is negligible for micrometric pore sizes. Metzger and Tsotsas [55] stated that the potential reduction in vapor pressure above the curved liquid-gas interface is negligible for micrometric pore sizes and should be considered for nanometric pores.

3.2 The Kinetic theory of evaporation

Condensation and evaporation processes have been studied extensively in the works of literature [56]. When condensation occurs at an interface, the flux of vapor molecules into the liquid must exceed the flux of liquid molecules escaping to the vapor phase. When evaporation occurs, on the other hand, the flux of liquid molecules escaping to the vapor phase must exceed the flux of vapor molecules into the liquid. Schrage [57] used the kinetic theory of gases to describe condensation and evaporation processes and considered separately the fluxes of condensing and vaporizing molecules in each direction. From kinetic theory, the mass flow rate of molecules passing in either direction through an imagined plane is given by

$$\left|\dot{m}_{\delta}\right| = \sqrt{\frac{M_v}{2\pi R_u}}\frac{P}{\sqrt{T}}, \tag{3.2.1}$$

where $\dot{m}_{\delta}$ is the mass flux of molecules, M_v is the molecular mass of the vapor. The net molecular flux through an interface is

$$\dot{m}_{\delta} = \dot{m}_{\delta+} - \dot{m}_{\delta-}. \tag{3.2.2}$$

Silver and Simpson [58] estimated the correction factor by assuming moderate and high temperatures and applied ideal gas law for the equilibrium vapor density, leading to an explicit relation for the mass flux at the interface for evaporation,

$$\dot{m}_{evp} = \frac{2\alpha}{2-\alpha}\sqrt{\frac{M_v}{2\pi R_u}}\left(\frac{P_l}{\sqrt{T_l}} - \frac{P_{\mathrm{v}}}{\sqrt{T_{\mathrm{v}}}}\right). \tag{3.2.3}$$

The evaporation mass flux equation (3.2.3) is referred to as the Kucherov-Rikenglaz equation [59] and it can be used for non-equilibrium evaporation. α is the accommodation coefficient [60]. The values of α obtained by different researchers are all close to unity. Mills [61] recommended that α should be less than unity when the working fluid or the interface is contaminated. P_l is the liquid pressure and P_v is the pressure of the vapor; in the case of a vapor mixture such as air, P_v is the partial pressure of the liquid vapor in the air mixture. Partial pressure is calculated as $P_v = cP_{air}$, where c is the substance's vapor mole fraction in the air mixture at the interface and P_{air} is air pressure on the interface.

If we assume that the interface temperature is continuous, and consistent with the temperature in the environment, i.e. $T_l = T_{\mathrm{v}} = T_s$ (a subscript "s" stands for a quantity valued at the interface), then equation (3.2.3) gives the net evaporation rate as

$$\dot{m}_{evp} = \frac{2\alpha}{2-\alpha}\sqrt{\frac{M_v}{2\pi R_u T_s}}\left(P_l - P_v\right) = \frac{2\alpha}{2-\alpha}\sqrt{\frac{M_v}{2\pi R_u T_s}}\left(P_l - c_s P_{air}\right). \tag{3.2.4}$$

It is noted that some authors believe that there is a temperature jump at the phase change interface (e.g. Badam et al. [62]). Gatapova et al. [63] studied the temperature jump at water-air interface during evaporation. The measured temperature profiles agree qualitatively with the results obtained by kinetic theory. It is observed that the value of temperature jump at the interface increases with greater heat flux added to the water layer. The temperature jump is negligible at room temperature based on their experiments. It is also noted that some authors have replaced the liquid side pressure P_l with the saturation vapor pressure for a flat interface [62]. Such a practice by itself compromises and weakens their claim that the interface temperature experiences a jump. For simplicity, we will assume that the interface temperature is continuous and use equation (3.2.4) for the evaporation rate. The kinetic equation (3.2.3) will be used in the cases when the full thermal effect is considered without assuming temperature continuity at the interface such as the liquid phase is heated.

A further simplification is attempted by considering the momentum balance equation at the phase changing interface in the normal direction [64],

$$\dot{m}\left[\!\left[\mathbf{v}\right]\!\right] + \left[\!\left[\mathbf{T}\right]\!\right]\mathbf{n}_{12} = 2H\sigma\mathbf{n}_{12}, \tag{3.2.5}$$

where $\mathbf{n}_{12}$ points from the liquid side to the vapor side [65], and $[\![\ ]\!]$ stands for the jump in the quantity as we cross the interface from the liquid side to the vapor side. The right-hand side represents the capillary pressure. On the left-hand side, the first term represents the change of momentum as mass is transported across the interface. $\left[\!\left[\mathbf{T}\right]\!\right]\mathbf{n}_{12}$ represents the

net force per unit area acting on the interface. When neglecting the normal viscous stress term, the normal direction momentum balance equation at the interface can be written as

$$P_l - P_{air} = -\frac{2\sigma\cos\theta}{r} + \dot{m}^2\left(\frac{1}{\rho_{vap}} - \frac{1}{\rho_f}\right), \tag{3.2.6}$$

where ρ_f and ρ_{vap} are the density of the liquid fragrance and vapor fragrance at the evaporating interface. Assuming the evaporation rate is small enough, the change of momentum across the interface due to inertia can be neglected (the second term on the right-hand side of (3.2.6)). Thus, we have

$$P_l - P_{air} = -\frac{2\sigma\cos\theta}{r}. \tag{3.2.7}$$

When equation (3.2.7) is substituted into the kinetic theory formula (3.2.4), the evaporation rate can be expressed in terms of the air-side pressure:

$$\dot{m}_{evp} = \frac{2\alpha}{2-\alpha}\sqrt{\frac{M_v}{2\pi R_u T_s}}\left[\left(1-c_s\right)P_{air} - \frac{2\sigma\cos\theta}{r}\right] \tag{3.2.8}$$

Equation (3.2.8) indicates that when there is no fragrance vapor in the air, $c_s = 0$, the evaporation rate is the highest. As the concentration of the fragrance vapor in the air near the interface increases, it becomes harder to evaporate with a liquid-wetted interface. Thus, one should avoid using extremely small pore-size pads, as the liquid fragrance can easily get clogged by the capillary effect, resulting in no evaporation at all. This has to be balanced against the fact that it is easier to draw up the liquid from the bottle for pads with smaller pores which give rise to larger capillary suction. It is noted that when the air is modeled as an ideal gas, the right-hand-side of equation (3.2.8) can be written as

$\frac{2\alpha}{2-\alpha}\sqrt{\frac{M_v}{2\pi R_u}}\left[\left(1-c_s\right)\rho\frac{R_u}{M_v}\sqrt{T_s}-\frac{2\sigma\cos\theta}{r\sqrt{T_s}}\right]$. This indicates that high temperature promotes evaporation. In our simulation, we have assumed the temperature remains constant. Thus, the effect of non-uniform temperature is neglected.

It is observed that by ignoring the inertial effect, equation (3.2.8) under-estimates the evaporation rate. However, keeping the inertial effect in the model complicates the problem significantly, as the evaporation rate equation becomes quadratic in the evaporation rate. Yet another approach to obtain the liquid pressure at the interface in the evaporation rate equation (3.2.4) is to obtain the liquid pressure in the pad via the dynamic equations within the pad. This topic will be picked up in Chapter 4 below.

CHAPTER 4

DYNAMIC WICKING AND COUPLING TO EVAPORATION

In this chapter, we develop a new dynamic wicking model based on the passive air freshener designed by Henkel and discuss its coupling to the surface evaporation from the wetted pad.

4.1 Surface boundary condition and the vertical flow inside the pad

As discussed in Chapter 2, it is observed from the simulation and experimental results that the liquid front inside the evaporation pad rises evenly (horizontal front on the macro-scale) after a short-time initial effect. Thus, it is reasonable to assume that the front is horizontal when the pores are uniformly distributed with a constant porosity, as shown in Figure 9. We further assume that the pressure inside the wicking pad is uniform at any horizontal level.

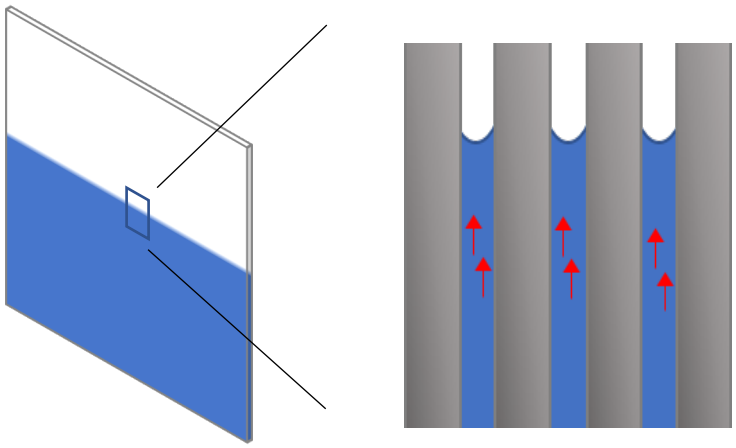

(a) Macro-scale. (b) Pore-scale

Fig 9. The ideal liquid wicking process in microfiber material, modeled by a bundle of capillary tubes. The curved surface on the pore-scale is undetectable on the macro-scale.

From the evaporation rate equation for a single capillary tube, equation (3.2.4), the rate of evaporation from a unit porous surface area (wetted side surface) is:

$$\dot{m}_{evp} = \phi \frac{2\alpha}{2-\alpha} \sqrt{\frac{M_v}{2\pi R_u T_s}} \left(\overline{p}_l - c_s P_{air} \right), \tag{4.1.1}$$

where ϕ is the porosity of the pad and the average liquid pressure is used in (4.1.1). This evaporation rate is a function of the vertical position z.

Figure 10 shows the schematic of fragrance evaporation from a wicking pad with a thickness of $2H$ across the pad. The pores are uniformly distributed at the evaporation surface and assume the mean radius of all the pores is r. The evaporation rate can also be computed from the diffusive flux of mass fraction at the surface of the evaporation pad shown in Figure 10:

$$\dot{m} = -D_e \rho_{vap} \left. \frac{\partial c}{\partial x} \right|_{x=H}, \tag{4.1.2}$$

where D_e is the effective diffusion coefficient of the fragrance vapor in the air, c is the mass fraction of the fragrance vapor in the air.

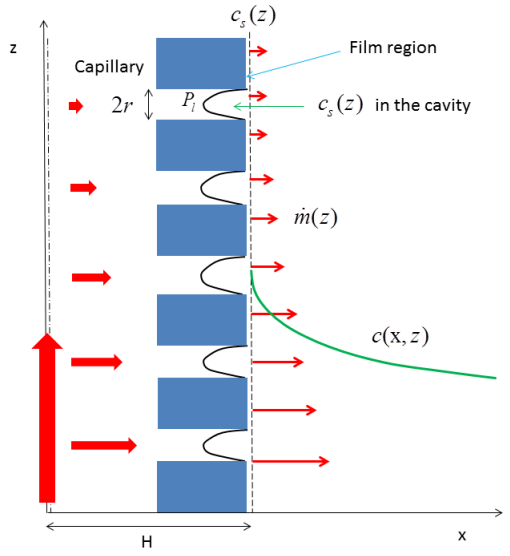

Fig. 10 Schematic of fragrance evaporation through a porous surface in cross-sectional view. The figure shows one-half of the pad cross-section. 2H is the thickness of the pad.

At the boundary $x=H$, the evaporation rate is then

$$\phi\left(\frac{2\alpha}{2-\alpha}\right)\sqrt{\frac{M_v}{2\pi R_u T_s}}\left[\overline{p}_l - c\Big|_{x=H} P_{air}\right] = -D_e \rho_{vap} \frac{\partial c}{\partial x}\Big|_{x=H}. \tag{4.1.3}$$

This will be the boundary condition used on the porous pad surface for the concentration field and the air pressure outside the wick. This boundary condition couples the wicking dynamic inside the pad-bottle system to the mass transport outside the pad.

Now consider the capillary suction driven flow inside the pad shown in Figure 10. The vertical flow inside the wick is a Poiseuille-like flow with mass leaking from the sides of the pad surfaces. The conservation of mass equation for an incompressible fluid, written in terms of the Darcy velocity, is

$$\frac{\partial u}{\partial x} + \frac{\partial w}{\partial z} = 0. \tag{4.1.4}$$

Integrating this equation across the wick thickness along the x-axis and utilizing the symmetric condition at the centerline leads to

$$H\frac{\partial \overline{w}}{\partial z} + u\Big|_{x=H} = 0, \tag{4.1.5}$$

where $\overline{w}$ stands for the thickness-averaged vertical velocity component and $u\Big|_{x=H}$ is the horizontal velocity at the pad surface. If the density of the fragrance is ρ_f, the mass flux delivered by the vertical flow within the wick at any height is given by Darcy's law:

$$\overline{w} = -\frac{\kappa}{\mu}\left(\frac{\partial \overline{p}_l}{\partial z} + \rho_f g\right). \tag{4.1.6}$$

Since $u\Big|_{x=H}$ in (4.1.5) is the evaporation velocity vertical from the pad surface, it is given

by the evaporation rate via the relation $u\big|_{x=H} = \dfrac{\dot{m}(z)}{\rho_f}$. Substituting this relation into (4.1.5) gives us

$$\frac{\partial \overline{w}}{\partial z} = -\frac{\dot{m}\left(z\right)}{\rho_f H}. \tag{4.1.7}$$

This implies that as the liquid travels upward within the wick, the vertical velocity decreases due to evaporation. Substituting (4.1.6) into (4.1.7), we obtained the relationship between the averaged pressure equation inside the wick and evaporation rate:

$$\frac{\partial^2 \overline{p}_l}{\partial z^2} = \frac{\mu}{\kappa}\frac{\dot{m}(z)}{\rho_f H}. \tag{4.1.8}$$

Now consider the top meniscus inside the wick at any time. If the maximum height the fragrance liquid can travel upward to is $z = z_T\left(t\right)$, the averaged vertical velocity at this top can be calculated by Darcy's law (4.1.6) as well as the time derivative of $z_T\left(t\right)$:

$$\overline{w}\Big|_{z=z_T(t)} = -\frac{\kappa}{\mu}\left(\frac{\partial \overline{p}_l}{\partial z}\bigg|_{z=z_T(t)} + \rho_f g \right) = \phi \frac{dz_T}{dt}. \tag{4.1.9}$$

The quantity $-\dfrac{dz_T}{dt}$ measures how fast the top meniscus decreases in time after reaching the highest point. Similarly, we apply Darcy's law to the bottom of the wicking pad $\left(z = d_0^+\right)$ to get the mean vertical entrance velocity of the liquid:

$$\overline{w}\Big|_{z=d_0^+} = -\frac{\kappa}{\mu}\left(\frac{\partial \overline{p}_l}{\partial z}\bigg|_{z=d_0^+} + \rho_f g \right). \tag{4.1.10}$$

In the sections below, the velocity of the top meniscus and the liquid pressure profile along the evaporation pad will be discussed. In our model, the level of the liquid fragrance in the container varies obviously during the wicking process. The decreasing rate of the liquid level will also be included in our analysis.

4.2 Mass balance equation

Pertinent to the more specific geometric model depicted in Figure 11, the liquid fragrance is pulled upward by capillary force through a thin $b_0 \times d_0 \times 2H$ stem to the wicking pad with the size of $b \times d \times 2H$. The initial liquid fragrance volume in the bottle is $V(0) = A_0 h(0) - (1-\phi) 2Hb_0 h(0)$, where A_0 is the bottom area of the container, ϕ is the porosity of the wicking material.

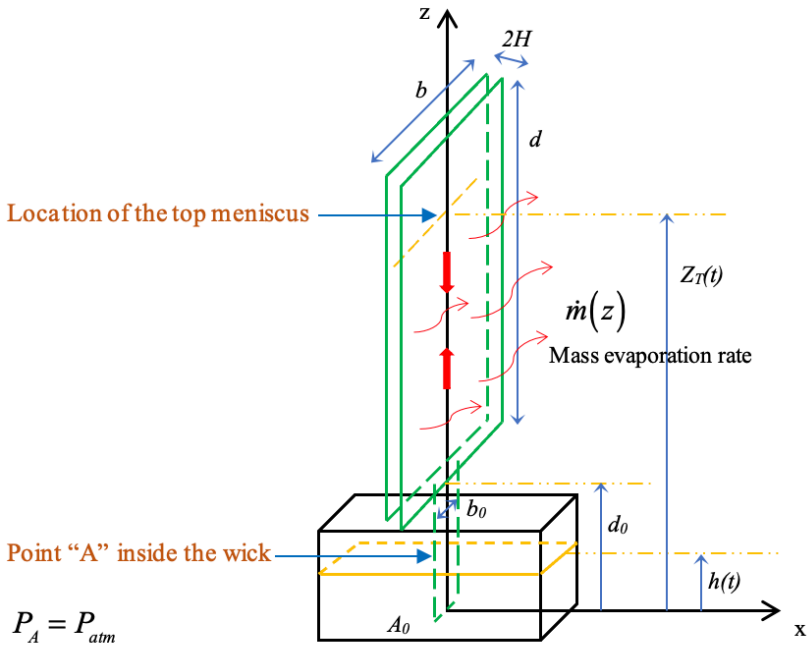

Fig. 11 schematic of dynamic wicking with evaporation.

At any time *t*, the level of the liquid fragrance inside the bottle is $h(t)$, the location of the top meniscus is at $z_T(t)$. Total liquid fragrance volume is:

$$\begin{aligned} V_{Total}(t) &= A_0 h(t) - (1-\phi)2Hb_0 h(t) + \phi 2Hb_0(d_0 - h(t)) + \phi 2Hb\left[z_T(t) - d_0\right] \\ &= (A_0 - 2Hb_0)h(t) + \phi 2Hb_0 d_0 + \phi 2Hb\left[z_T(t) - d_0\right]. \end{aligned} \tag{4.2.1}$$

The total mass of the liquid fragrance at time t is

$$M_{Total}(t) = \rho_f V_{Total}(t). \tag{4.2.2}$$

Mass conservation for the fragrance requires

$$\frac{\partial M_{Total}(t)}{\partial t} + \oiint_{evaporating\ surface} \rho_f \mathbf{v} \bullet \mathbf{n} da = 0. \tag{4.2.3}$$

This gives the equation that relates the velocity of the top meniscus and the variation of the liquid fragrance level inside the bottle:

$$(A_0 - 2Hb_0)\frac{dh}{dt} + 2b\phi H\frac{dz_T}{dt} + \frac{\dot{M}(t)}{\rho_f} = 0, \tag{4.2.4}$$

where

$$\dot{M}(t) = 2b\int_{d_0}^{z_T(t)} \dot{m}(z)\,dz \ \ (\geq 0) \tag{4.2.5}$$

is the total evaporation rate over the 2-sides of the wick surfaces at any time. Obviously, $h(t)$ depends on $z_T(t)$ and $\dot{m}(z)$. Further analysis is needed to compute the liquid level inside the bottle.

The same analysis can be applied to the fragrance inside the container (bottle): the mass of the fragrance inside the container at any time is

$$M_{container} = \rho_f\left[A_0 h(t) - 2Hb_0 h(t) + \phi 2Hb_0 d_0\right]. \tag{4.2.6}$$

Conservation of the fragrance mass inside the container gives

$$\frac{dM_{container}}{dt} = -\rho_f 2Hb_0 \left.\overline{w}\right|_{d_0^-}, \tag{4.2.7}$$

where $\left.\overline{w}\right|_{h_0^-}$ is the average vertical velocity at the top of the stem. The above equation can also be written as a function of the rate of the variation of the liquid level inside the container:

$$\left(A_0 - 2Hb_0\right)\frac{dh}{dt} = -2Hb_0 \left.\overline{w}\right|_{d_0^-}. \tag{4.2.8}$$

Since the mass flow rate across the top of the stem is the same as the mass flux starting from the bottom of the pad,

$$\rho_f 2Hb_0 \left.\overline{w}\right|_{d_0^-} = \rho_f 2Hb \left.\overline{w}\right|_{d_0^+}. \tag{4.2.9}$$

Thus, we have

$$b_0 \left.\overline{w}\right|_{d_0^-} = b \left.\overline{w}\right|_{d_0^+}. \tag{4.2.10}$$

Substituting (4.2.10) into the mass conservation equation. (4.2.8), the mean vertical velocity at the bottom of the pad becomes:

$$\left.\overline{w}\right|_{d_0^+} = -\frac{A_0 - 2Hb_0}{2Hb}\frac{dh}{dt}. \tag{4.2.11}$$

Apply Darcy's law to the fluid in the wicking pad, then we have the pressure gradient at the bottom of the pad:

$$\left.\frac{\partial \overline{p}_l}{\partial z}\right|_{z=d_0^+} = -\rho_f g - \frac{\mu}{\kappa}\left.\overline{w}\right|_{z=d_0^+} = -\rho_f g + \frac{\mu}{\kappa}\frac{A_0 - 2Hb_0}{2Hb}\frac{dh}{dt}. \tag{4.2.12}$$

Integrate equation (4.1.8)

$$\frac{\partial^2 \overline{p}_l}{\partial z^2} = \frac{\mu}{\kappa} \frac{\dot{m}(z)}{\rho_f H}$$

over the wetted portion of the wicking pad from d_0 to $z_T(t)$:

$$\left.\frac{\partial \overline{p}_l}{\partial z}\right|_{z=z_T(t)} - \left.\frac{\partial \overline{p}_l}{\partial z}\right|_{z=d_0} = \frac{\mu}{\kappa} \frac{1}{\rho_f H} \int_{d_0}^{z_T(t)} \dot{m}(z)\, dz = \frac{\mu}{\kappa} \frac{\dot{M}(t)}{2\rho_f bH}. \tag{4.2.13}$$

Substituting (4.1.9) and (4.2.12) into (4.2.13) gives us:

$$-\phi \frac{dz_T}{dt} - \frac{A_0 - 2Hb_0}{2Hb} \frac{dh}{dt} = \frac{\dot{M}(t)}{2\rho_f bH}. \tag{4.2.14}$$

This equation is identical to equation (4.2.4). This shows the consistency of the approach used. In the next section, the liquid pressure inside the wicking pad is discussed, and the equations needed to obtain $z_T(t)$ and $h(t)$ are obtained after that.

4.3 Pressure profile inside the wick

More analysis is performed to explore the liquid pressure at any height inside the evaporation pad, which is needed to extract the mass flux at the evaporation surface. Integrate equation (4.1.8)

$$\frac{\partial^2 \overline{p}_l}{\partial z^2} = \frac{\mu}{\kappa} \frac{\dot{m}(z)}{\rho_f H}$$

along the evaporation pad from the bottom $z=d_0$ to any height under the top meniscus:

$$\frac{\partial \overline{p}_l}{\partial z} - \left.\frac{\partial \overline{p}_l}{\partial z}\right|_{z=d_0} = \frac{\mu}{\kappa} \frac{1}{\rho_f H} \int_{d_0}^{z} \dot{m}(z)\, dz. \tag{4.3.1}$$

Substituting the expression for the pressure gradient at $z=d_0$ (4.2.12) into this equation results in

$$\frac{\partial \overline{p}_l}{\partial z} = -\rho_f g + \frac{\mu}{\kappa}\frac{A_0 - 2Hb_0}{2Hb}\frac{dh}{dt} + \frac{\mu}{\kappa}\frac{1}{\rho_f H}\int_{d_0}^{z} \dot{m}(\xi)\, d\xi. \tag{4.3.2}$$

Equation (4.3.2) indicates that evaporation causes the liquid pressure to increase in the z-direction. This effect can be considered as an effective reduction of the gravitational pull down on capillary rise. In other words, evaporation enhances capillary rise, or evaporation draws liquid up the pad against gravity.

Integrating (4.3.2) from z to $z_T(t)$ gives

$$\overline{p}_l(z) = \overline{p}_l\big|_{z_T(t)} - \left[-\rho_f g + \frac{\mu}{\kappa}\frac{A_0 - 2Hb_0}{2Hb}\frac{dh}{dt}\right]\left(z_T(t) - z\right) - \frac{\mu}{\kappa}\frac{1}{\rho_f H}\int_{z}^{z_T(t)}\int_{d_0}^{\eta} \dot{m}(\xi)\, d\xi d\eta. \tag{4.3.3}$$

Here we assume that the pressure just above the top meniscus is the local air pressure which is taken as atmospheric. Thus, the averaged pressure profile inside the wicking pad is:

$$\overline{p}_l(z) = P_{atm} - \frac{2\sigma\cos\theta}{r} + \left[\rho_f g - \frac{\mu}{\kappa}\frac{A_0 - 2Hb_0}{2Hb}\frac{dh}{dt}\right]\left(z_T(t) - z\right) - \frac{\mu}{\kappa}\frac{1}{\rho_f H}\int_{z}^{z_T(t)}\int_{d_0}^{\eta} \dot{m}(\xi)\, d\xi d\eta \tag{4.3.4}$$
$$d_0 \le z \le z_T(t)$$

To obtain another expression with the liquid level in the container, consider Darcy's law in the stem. The Darcy velocity at $z = d_0^-$ is

$$\overline{w}\big|_{d_0^-} = -\frac{\kappa}{\mu}\left(\left.\frac{\partial \overline{p}_l}{\partial z}\right|_{z=d_0^-} + \rho_f g\right) \approx -\frac{\kappa}{\mu}\left(\frac{\overline{p}_l\big|_{z=d_0^-} - P_{atm}}{d_0 - h(t)} + \rho_f g\right). \tag{4.3.5}$$

It is assumed that the pressure gradient at the top of the stem is simply the pressure difference between the top of the stem and the location contact with the fragrance level divided by the distance. Substituting (4.3.5) into (4.2.8)

$$\left(A_0 - 2Hb_0\right)\frac{dh}{dt} = -2Hb_0\,\overline{w}\Big|_{d_0^-},$$

we obtained the average pressure at the entrance to the pad:

$$\overline{p}_l\Big|_{z=d_0^-} = P_{atm} - \left[\rho_f g - \frac{\mu}{\kappa}\frac{A_0 - 2Hb_0}{2Hb_0}\frac{dh}{dt}\right]\left(d_0 - h(t)\right). \tag{4.3.6}$$

Assume the average pressure at the entrance is the same as the average pressure at the bottom of the evaporation pad, i.e., $\overline{p}\Big|_{z=d_0^-} = \overline{p}\Big|_{z=d_0^+}$. Based on the pressure expressions (4.3.4) and (4.3.6), we obtain another expression for the variation of the liquid height:

$$\begin{aligned}&\rho_f g\left[z_T(t) - h(t)\right] - \frac{2\sigma\cos\theta}{r}\\ &= \frac{\mu}{\kappa}\frac{A_0 - 2Hb_0}{2H}\left(\frac{z_T(t) - d_0}{b} + \frac{d_0 - h(t)}{b_0}\right)\frac{dh}{dt} + \frac{\mu}{\kappa}\frac{1}{\rho_f H}\int_z^{z_T(t)}\int_{d_0}^{\eta}\dot{m}(\xi)\,d\xi\,d\eta.\end{aligned} \tag{4.3.7}$$

Thus, besides equation (4.2.14)

$$-\phi\frac{dz_T}{dt} - \frac{A_0 - 2Hb_0}{2Hb}\frac{dh}{dt} = \frac{\dot{M}(t)}{2\rho_f bH},$$

we have another equation for $z_T(t)$ and $h(t)$. Rewriting the double integral, we have

$$\begin{aligned}&\frac{A_0 - 2Hb_0}{2H}\left(\frac{z_T(t) - d_0}{b} + \frac{d_0 - h(t)}{b_0}\right)\frac{dh}{dt}\\ &= \frac{\kappa}{\mu}\rho_f g\left[z_T(t) - h(t)\right] - \frac{\kappa}{\mu}\frac{2\sigma\cos\theta}{r} - \frac{1}{\rho_f H}\int_{d_0}^{z_T(t)}\dot{m}(\xi)\left[z_T(t) - \xi\right]d\xi.\end{aligned} \tag{4.3.8}$$

4.4 Summary of equations

A dynamic wicking model is proposed for a passive air freshener which has a rectangular evaporation pad with an inconspicuous 2D effect and a thin stem that absorbs liquid fragrance from a small container. The wicking velocity and the decreasing velocity

of the liquid in the bottle can be obtained. The liquid pressure inside the wick at any level is:

$$\begin{aligned}\overline{p}_l(z) &= P_{atm} - \frac{2\sigma\cos\theta}{r} + \left[\rho_f g - \frac{\mu}{\kappa}\frac{A_0 - 2Hb_0}{2Hb}\frac{dh}{dt}\right]\left(z_T(t) - z\right) \\ &- \frac{\mu}{\kappa}\frac{1}{\rho_f H}\left\{\left[z_T(t) - z\right]\int_{d_0}^{z}\dot{m}(\xi)\,d\xi + \int_{z}^{z_T(t)}\dot{m}(\xi)\left[z_T(t) - z\right]d\xi\right\}, d_0 \le z \le z_T\left(t\right).\end{aligned} \tag{4.4.1}$$

The height equations are:

$$\phi\frac{dz_T}{dt} + \frac{A_0 - 2Hb_0}{2Hb}\frac{dh}{dt} = -\frac{1}{\rho_f H}\int_{d_0}^{z_T(t)}\dot{m}\left(\xi\right)d\xi, \tag{4.4.2}$$

$$\begin{aligned}&\frac{A_0 - 2Hb_0}{2H}\left(\frac{z_T(t) - d_0}{b} + \frac{d_0 - h\left(t\right)}{b_0}\right)\frac{dh}{dt} \\ &= \frac{\kappa}{\mu}\rho_f g\left[z_T\left(t\right) - h\left(t\right)\right] - \frac{\kappa}{\mu}\frac{2\sigma\cos\theta}{r} - \frac{1}{\rho_f H}\int_{d_0}^{z_T(t)}\dot{m}\left(\xi\right)\left[z_T\left(t\right) - \xi\right]d\xi.\end{aligned} \tag{4.4.3}$$

The mass flux equation at the surface of the evaporation pad is:

$$\dot{m} = \phi\left(\frac{2\alpha}{2-\alpha}\right)\sqrt{\frac{M_v}{2\pi R_u T_s}}\left[\overline{p}_l - c\big|_{x=H}P_{air}\right] = -D_e\frac{\partial C_m}{\partial x}\bigg|_{x=H}. \tag{4.4.4}$$

Consider the special case where $b = b_0$, eliminating $\frac{dh}{dt}$ from the 2 differential equations (4.4.2) and (4.4.3), we have

$$\begin{aligned}&\phi\frac{dz_T}{dt} + \frac{\kappa}{\mu}\rho_f g + \frac{1}{\rho_f H}\int_{d_0}^{z_T(t)}\dot{m}\left(\xi\right)d\xi \\ &= \frac{\kappa}{\mu}\frac{2\sigma\cos\theta}{r}\frac{1}{z_T\left(t\right) - d_0} + \frac{1}{\rho_f H}\frac{1}{z_T\left(t\right) - d_0}\int_{d_0}^{z_T(t)}\dot{m}\left(\xi\right)\left[z_T\left(t\right) - \xi\right]d\xi.\end{aligned} \tag{4.4.5}$$

This is the equivalent of the Washburn equation [66] for a porous medium with an

evaporating surface ($\phi = 1$ and $\kappa = \frac{r^2}{8}$ for an empty cylindrical pore). Although the above equations are derived for the specific geometries and configurations of the air freshener, the same method can be applied to derive similar equations for more general geometries and configurations.

CHAPTER 5

EXPERIMENTS PERFORMED BY HENKEL

Henkel USA in Scottsdale, Arizona, has performed experiments on their passive air freshener performance shown in Figure 12. A 1.2mm-thick microfiber-made multi-ply paper board is used as a wick. The dimension is 6cm x 10cm and 1cm x 4cm for the stem. The porosity of the wicking pad is 60% and the material holding capacity for the fragrance sample is about 0.087g/cm^2. Half of the stem is immersed in the liquid fragrance initially and reaches down to the bottom of the container. The fragrance is filled in a 2cm height container. The properties of the fragrance and the wicking pad are listed in Table 1 and Table 2 in Chapter 2.

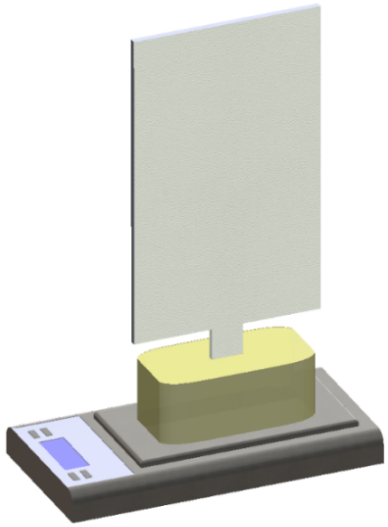

Fig. 12 The wicking sample and weight scale used in the experiment.

In the first experiment, the air freshener sample, as well as the weight scale, are placed at the center of a $37\text{cm} \times 35\text{cm} \times 46\text{cm}$ chamber as shown in Figure 13. The lid of the chamber is cracked open on the top to allow air release while preventing noticeable airflow

inside the chamber. The chamber was placed in a room at a constant temperature of 68°F and away from any meaningful airflow. The weight data of the unit was collected every few hours. The weight loss of the whole unit will be the evaporated mass from the two surfaces of the pad.

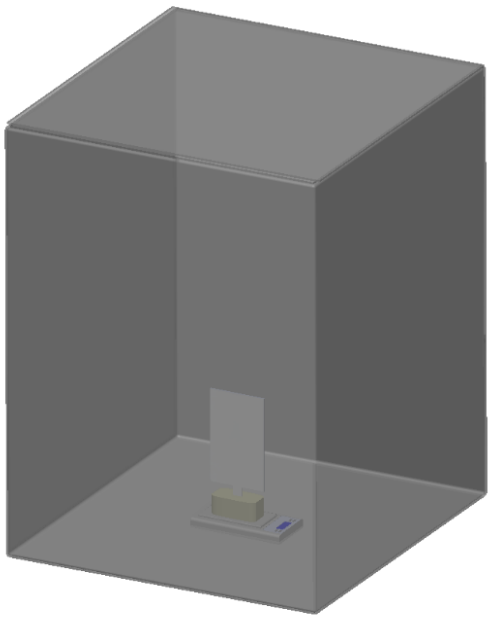

Fig. 13 The unit is placed at the center of a chamber.

The data of weight loss of fragrance with time is listed in Table 3 and plotted as Figure 14. It is observed that the fragrance wets the entire wicking pad in one hour and 28 minutes. The weight lost 0.04g by then.

Table 3. Experimental Data for the Sample Placed in a Chamber

Total time (hours)	0	15	42	91	210	328	375
Weight loss (g)	0	0.18	0.49	0.96	2.19	3.20	3.51
Evaporation rate (mg/hr)	0	12.0	11.5	9.6	10.3	8.6	6.6

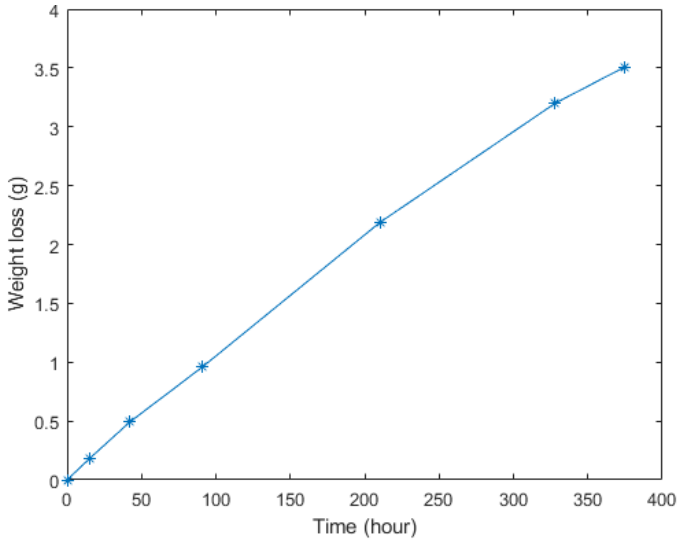

Fig 14. The growth of weight loss of the sample placed in a chamber with time.

It is observed from Table 3 and Figure 14 that the evaporation rate decreased with time. As more of the fragrance vapor evaporates out, the higher concentration of fragrance in the chamber may lower the evaporation rate. In the second experiment, the sample unit is placed in an empty lab with dimensions of $13\text{ft} \times 10\text{ft} \times 7\text{ft}$ shown in Figure 15.

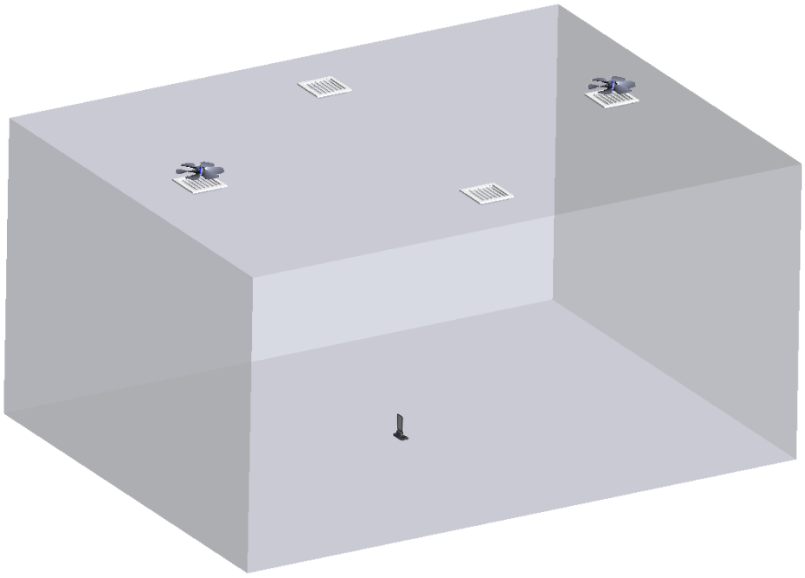

Fig. 15 The unit is placed in a room with dimensions of $13\text{ft} \times 10\text{ft} \times 7\text{ft}$.

The properties of the fragrance and dimensions of the wicking pad are the same as in the previous experiment. The wick pad porosity is 60%. The room temperature is kept at 68°F. The fan of the intake air vent is always on. Exhaust air vents are mounted on the ceiling as well, but the fan is off. The air freshener unit is placed in the center of the lab to avoid direct wind from the intake air vent. Based on the standard of ASHRAE (American Society of Heating, Refrigerating and Air-Conditioning Engineers [38]) in 2019, the minimum ventilation airflow rate per unit area for office buildings is 0.3~0.6L/s.m^2. This implies that the total airflow from the inlets is approximately 5.0L/s. For a typical 8'x8' vent, the velocity is at least 0.0625m/s. The data for the second experiment is shown in Table 4 and plotted in Figure 16.

Table 4. Experiment Data for the Sample Placed in a Room

Total time (hours)	0	15	42	91	210	328	375
Weight loss (g)	0	0.45	1.3	2.6	5.68	8.52	9.42
Evaporation rate (mg/hr)	0	30.0	31.5	26.5	25.9	24.1	19.1

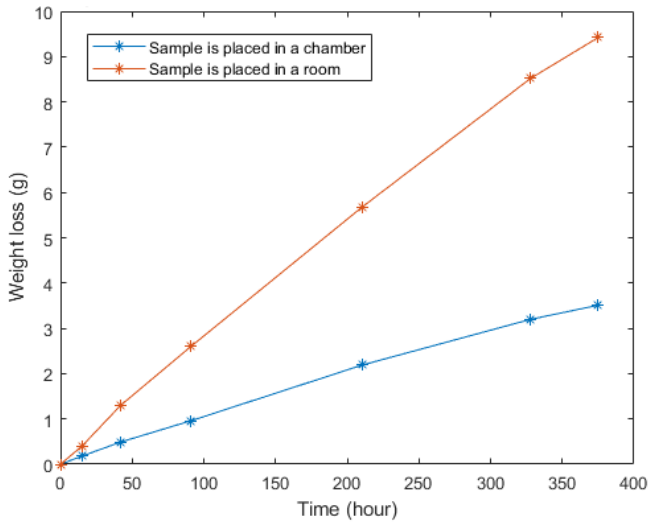

Fig. 16 The growth of weight loss of the samples placed in or without a chamber.

The weight loss of the sample placed in a room is higher compared to the one placed in a chamber, which indicates that the airflow in the environment highly affected the evaporation rate.

CHAPTER 6

MODEL PREDICTION AND COMPARISON WITH EXPERIMENTS

In this chapter, we discuss the performance of various models as they compared to the experiments.

6.1 Wicking process with a constant evaporation rate

The capillary model that includes the evaporation effect built by Fries et al. [5] is widely used by many researchers. The evaporation rate is assumed to be constant in their study. In this section, Fries' model is used to predict the highest capillary rise for the air freshener designed by Henkel. Assuming the wick is high enough and the transport of the liquid vapor away from the wicking pad is not restricted by the buildup of a boundary layer, Fries et al. state that the flow velocity in the wicking pad is composed of two parts, the liquid front velocity $\dot{z}_T$ and the refill velocity to refill the evaporated liquid, v_r [5]. The refill velocity is height dependent and reaches the maximum value at the bottom of the wicking pad.

$$v_{r,0} = \frac{\dot{M}_e}{\phi b H \rho_f} = \frac{\dot{m}_e \cdot 2b \cdot z_T}{\phi b H \rho_f} = \frac{2\dot{m}_e z_T}{\phi H \rho_f}, \tag{6.1.1}$$

where $\dot{m}_e$ is the evaporation rate, $\dot{M}_e$ is the total mass flow from both sides of the pad due to evaporation. b and H are the width and thickness of the wicking pad. ρ_f is the density of the fragrance liquid. The momentum balance of the liquid inside the wicking pad gives

$$\frac{2\sigma\cos\theta}{R_s} = \rho_f g z_T + \frac{\phi}{\kappa}\mu z_T \dot{z}_T + \frac{\mu \dot{m}_e}{\kappa \rho_f H} {z_T}^2. \tag{6.1.2}$$

The last term refers to the viscous pressure loss due to the velocity refill velocity to refill

the evaporated liquid. Setting $\dot{z}_T = 0$, the highest point where the fragrance can reach is estimated as:

$$z_{T,\max} = -\frac{\kappa\rho_f^2 gH}{2\mu\dot{m}_e} + \sqrt{\left(\frac{\kappa\rho_f^2 gH}{2\mu\dot{m}_e}\right)^2 + \frac{\kappa\rho_f H}{\mu\dot{m}_e}\frac{2\sigma\cos\theta}{R_s}}. \tag{6.1.3}$$

Applying the properties of the fragrance and the wicking pad to (6.1.3) and assuming the evaporation rate is constant and equals 12mg/h, the highest evaporation rate obtained from the experiment without airflow, it's calculated that the maximum height reachable is $z_{T,\max} = 0.63m$. This result is much higher than the height of the wick used in our experiment, which implies that the wicking pad used in the experiment will be always fully soaked with the fragrance.

The dynamic wicking model we introduced in Chapter 4 can be used to simulate the wicking process for our system. Figure 17 shows how the wicking height reaches the top bound for our model with a constant 12mg/h evaporation rate. It is solved by combining the height equations (4.4.2) and (4.4.3). At the first stage where the fluid flows in the 1cm-wide-stem, the Washburn equation is used to obtain the wicking height. Comparing Figure 17 with the 2D simulation result, the increase of the wicking height with time is no longer linear due to evaporation. The time needed to fully wet the wicking pad is closer to the experimental result described in Chapter 2. A longer time with experimental result indicates that the evaporation rate at the wicking process is higher than 12mg/h.

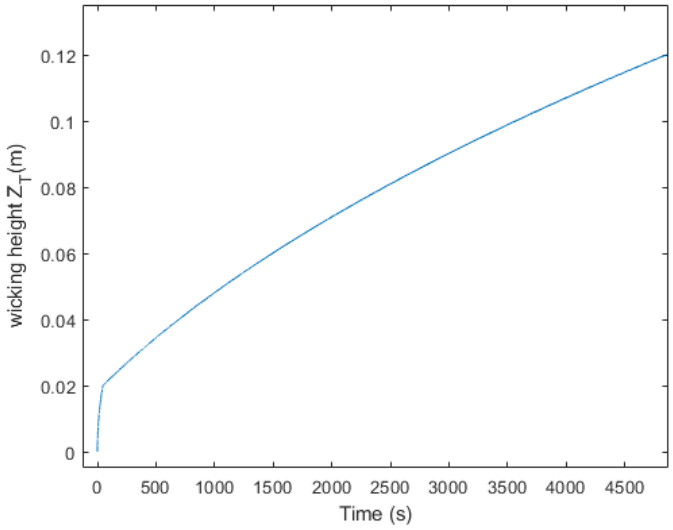

Fig.17 The increase of wicking height with time.

6.2 1D Numerical solution without buoyancy effect

We now consider the transport outside the pad. We start with the simplest model for the transport outside the pad: the transport of the fragrance outside the wick is diffusive only and the domain is unbounded. Furthermore, the diffusion in the vertical direction is neglected and the diffusion is in the horizontal direction only. This 1D model provides insight into the physics of evaporation.

Consider the concentration profile outside the wick. The 1D diffusion equation is

$$\frac{\partial c}{\partial t} = D_e \rho_{vap} \frac{\partial^2 c}{\partial x^2}, \tag{6.2.1}$$

where c is the mass fraction, D_e is the diffusion coefficient of the fragrance in the air. The initial condition is $c(x,0) = 0$. The boundary conditions are

$$\begin{aligned} &x = 0: \quad Ac - \frac{\partial c}{\partial x} = B, \\ &x \to \infty : c \to 0, \end{aligned} \tag{6.2.2}$$

where

$$A=\left(\frac{2\alpha}{2-\alpha}\right)\frac{\phi}{\rho_{vap}D_e}\sqrt{\frac{M_w}{2\pi R_u T_s}}P_{air},$$
$$B=\left(\frac{2\alpha}{2-\alpha}\right)\frac{\phi}{\rho_{vap}D_e}\sqrt{\frac{M_w}{2\pi R_u T_s}}\overline{p}_l. \tag{6.2.3}$$

The boundary condition at the surface of the evaporation pad is defined based on the mass flux equation (4.4.4). Based on (4.4.1), the liquid pressure $\overline{p}_l$ inside the wick changes on a much slower time scale compared to the change in the concentration outside the wick. To simplify the calculation, it is assumed that both parameters A and B are constant. The solution of the diffusion equation is given in terms of the complementary error function [67]:

$$c=\frac{B}{A}\left[erfc\left(\frac{x}{2\sqrt{D_e t}}\right)-e^{Ax+A^2D_e t}erfc\left(\frac{x}{2\sqrt{D_e t}}+A\sqrt{D_e t}\right)\right]. \tag{6.2.4}$$

The mass flux at the surface is derived as:

$$\dot{m}=-D_e\rho_{vap}\left.\frac{\partial c}{\partial x}\right|_{x=0}\approx\frac{\rho_{vap}\sqrt{D_e}}{\sqrt{\pi}}\frac{\overline{p}_l}{P_{air}}\frac{1}{\sqrt{t}}. \tag{6.2.5}$$

An iterative procedure is used and implemented with MATLAB. The initial $\overline{p}_l(z)$ for diffusion model is derived by eliminating evaporation from (4.4.1) and with z_T being constant which equals to the total height of the wick,

$$\overline{p}_l(z,0)=p_{atm}-\frac{2\sigma\cos\theta}{r}+\rho_f g\left(z_T-z\right). \tag{6.2.6}$$

For each time step, the evaporation flux is derived by (6.2.5) and is used to update $h(t)$

and the pressure profile along the wicking pad $\overline{p}_l(z)$ by (4.4.3) and (4.4.1).

A dimensionless analysis is applied to reduce computing costs. The simulation is run from t=0 to t=425 hours with a time step of 0.01s. The characteristic time scale is

$$t_c = d^2 / D_e \tag{6.2.7}$$

The variation of weight loss and the height of the liquid fragrance with time is obtained. Compared to the experiment data, the evaporation rate of the numerical solution is higher in the first few hours and then it decreases faster as shown in Figure 18. This indicates that the buoyancy effect in the air which was neglected in the current 1D diffusion model may significantly affect the evaporation rate. Figure 19 shows the decrease of the height of fragrance in the bottle with time.

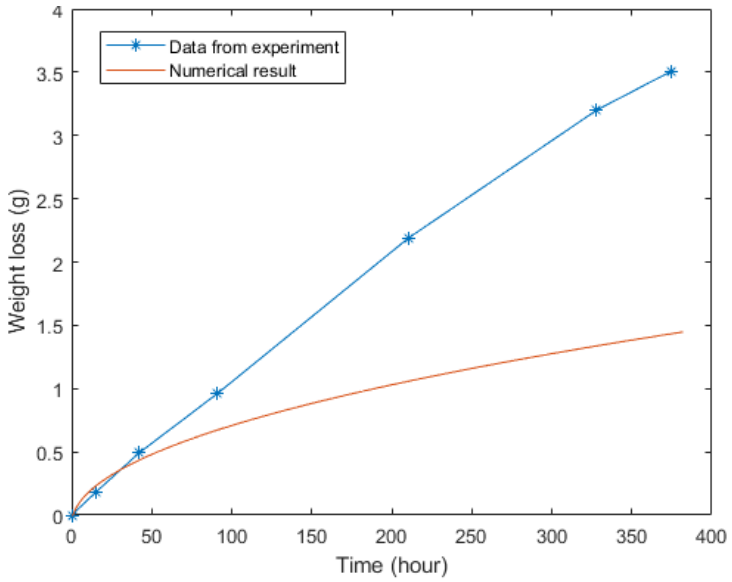

Fig. 18 Comparison of experiment data and 1D numerical result on weight loss.

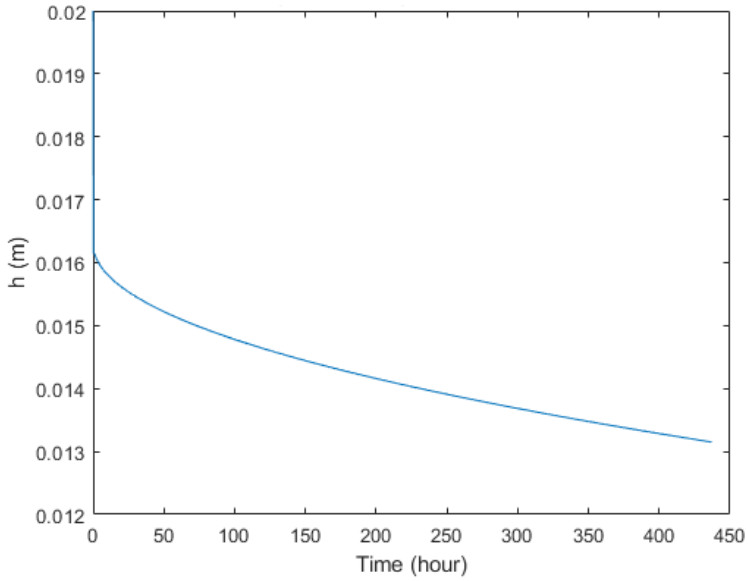

Fig. 19 Variation of the height of the liquid fragrance in the bottle derived from 1D analysis.

6.3 3D numerical solution with buoyancy effect

6.3.1 Model of fluid flow

After having mass diffusion considered, which is the transfer of mass due to a concentration gradient, mass convection is considered in this section. Fluid motion enhances mass transfer by removing the high-concentration fluid near the surface and replacing it with the lower-concentration fluid further away. The airflow immediately adjacent to the evaporating pad is driven by the natural convection from the buoyancy force, as the fragrance vapor is lighter than the ambient air. The non-uniform distribution of concentration of the fragrance component in the air leads to a density variation, which causes a rise of the air. A small change in density is accounted for as a volume force, which is introduced in the momentum equation in the opposite direction of gravity:

$$\rho\mathbf{g} - \nabla p = \rho\mathbf{g} - \nabla p_h - \nabla p_m = \left(\rho - \rho_\infty\right)\mathbf{g} - \nabla p_m, \tag{6.3.1}$$

where p_h is the hydrostatic pressure and p_m is the dynamic pressure. ρ_∞ is the density of the quiescent air away from the diffusion surface under room temperature. The density of air in the room is a function of both the fragrance concentration and temperature. In our study, the drops in both temperature and concentration are expected to be small. Thus, the density change can be considered linear. The Boussinesq approximation is used for the incompressible flow to linearize the density. The density of the ambient air with zero concentration of the fragrance is used as the reference density. The buoyancy term can be expanded as

$$\left(\rho-\rho_\infty\right)\mathbf{g}=-\rho_\infty\cdot\beta\left(T-T_\infty\right)\mathbf{g}-\rho_\infty\cdot\beta^*\left(C-C_\infty\right)\mathbf{g}, \tag{6.3.2}$$

where β^* is the volumetric coefficient of expansion with concentration, β is the volumetric coefficient of expansion with temperature. ρ_∞ is the reference density. T_∞ and C_∞ are the reference temperature and mass concentration. The dimensionless Grashof number approximates the ratio of the buoyancy force to the viscous force. The Grashof numbers for heat transfer and mass transfer, which correspond to the representative dimensionless values of the two terms on the right-hand-side of equation (6.3.2), are defined as

$$Gr_T=\frac{g\beta\left(T_s-T_\infty\right)L_c^3}{\nu^2},Gr_c=\frac{g\beta^*\left(C_s-C_\infty\right)L_c^3}{\nu^2}, \tag{6.3.3}$$

where ν is the kinematic viscosity, C_s is the mass concentration of the fragrance vapor at the liquid-vapor interface. For ideal gas, the coefficient of expansion with concentration can be calculated as [68]

$$\beta^* = -\frac{1}{\rho_\infty}\left(\frac{\partial \rho}{\partial c}\right)_{P,T} = \frac{1}{\rho_\infty}\left(\frac{Mw_a}{Mw_f} - 1\right), \tag{6.3.4}$$

where Mw_a and Mw_f are the molecular weight of air and the fragrance, respectively. The coefficient of expansion with temperature can be calculated as

$$\beta = -\frac{1}{\rho_\infty}\left(\frac{\partial \rho}{\partial T}\right)_{P,c}. \tag{6.3.5}$$

For an ideal gas, the thermal expansion coefficient equals to $\frac{1}{T_\infty}$. At room temperature, the value of the coefficient of expansion with concentration $\beta^* = 0.1306\frac{1}{\mathrm{K}}$, whereas the coefficient of expansion with temperature $\beta = 3.355\times10^{-3}\mathrm{m}^3/\mathrm{kg}$. Thus, the ratio of the two Grashof numbers is

$$\frac{Gr_T}{Gr_c} = \frac{\beta\left(T_s - T_\infty\right)}{\beta^*\left(c_s - c_\infty\right)} = 0.025\frac{\left(T_s - T_\infty\right)}{\left(c_s - c_\infty\right)}. \tag{6.3.6}$$

To estimate the evaporative temperature change in the fragrance liquid, a simple simulation coupled heat transfer and moisture transport in the air was implemented with an open container filled with water surrounded by an air domain. During evaporation, latent heat is released from the liquid surface and causes the temperature drop. The latent heat of vaporization of water is 2256kJ/kg [69]. The simulation result shows that the temperature drop is less than 1K with 20g water evaporated. Thus, the ratio of the Grashof number is smaller than 1. The heat convection can be neglected in our study to simplify the problem and to save computational costs. In addition, the heat transfer module in COMSOL is used to implement the mass transfer problem, which further reduced the computing cost. In order

to use the heat transfer module analogy for the mass transfer problem, the non-isothermal flow is set to have no heat source, no viscous dissipation, and no work done by pressure changes. The heat capacity and thermal conductivity are defined based on the heat/mass transfer analogy [70].

6.3.2 Governing equations

3D computational models were built based on the experiments. The numerical investigation of the natural buoyancy driven fluid flow and mass transfer in the chamber has been attempted. The simulations were conducted using the commercial CFD software COMSOL. Assuming the temperature is constant in the chamber and no heat transfer occurs. The time-dependent, isothermal, incompressible, and 3D form of the conservation equations was solved for the fluid flow in the chamber using the Boussinesq approximation. The dimensionless form of the continuity equation and momentum equations are:

$$\nabla \cdot \left(\overline{\mathbf{u}}\right) = 0, \tag{6.3.7}$$

$$\frac{\partial \overline{u}}{\partial t} + \left(\overline{u} \cdot \nabla\right)\overline{u} = -\frac{\partial \overline{P}}{\partial \overline{x}} + \frac{\mu}{\rho U_c L_c} \cdot \nabla^2 \overline{u}, \tag{6.3.8}$$

$$\frac{\partial \overline{v}}{\partial t} + \left(\overline{v} \cdot \nabla\right)\overline{v} = -\frac{\partial \overline{P}}{\partial \overline{y}} + \frac{\mu}{\rho U_c L_c} \cdot \nabla^2 \overline{v}, \tag{6.3.9}$$

$$\frac{\partial \overline{w}}{\partial t} + \left(\overline{w} \cdot \nabla\right)\overline{w} = -\frac{\partial \overline{P}}{\partial \overline{z}} + \frac{1}{\mathrm{Re}} \cdot \nabla^2 \overline{w} + \frac{Gr_c}{\mathrm{Re}^2} \cdot \overline{\theta}, \tag{6.3.10}$$

where $\overline{u}$, $\overline{v}$, and $\overline{w}$ are the dimensionless variables of the three components of the velocity. The characteristic length L_c is the height of the wicking pad d, the characteristic velocity $U_c = D_e/L_c$. The last term in the z-direction momentum equation represents the

buoyancy force, where $\bar{\theta} = \frac{C - C_\infty}{C_s - C_\infty}$ is the dimensionless term of the mass concentration.

The mass transport equation is:

$$\frac{\partial \bar{\theta}}{\partial \bar{t}} + \bar{u}\frac{\partial \bar{\theta}}{\partial \bar{x}} + \bar{v}\frac{\partial \bar{\theta}}{\partial \bar{y}} = \frac{D_e}{U_c L_c}\left[\frac{\partial^2 \bar{\theta}}{\partial \bar{x}^2} + \frac{\partial^2 \bar{\theta}}{\partial \bar{y}^2}\right]. \tag{6.3.11}$$

6.3.3 Boundary conditions and initial conditions

Figure 20 shows the working fluid domain for two different configurations based on the two experiments. The initial concentration is 0 in the fluid domain. Using the symmetry planes for each model removes 75% of the elements and reduces the computational time. The shapes of the fragrance container and weight scale are simplified as two blocks.

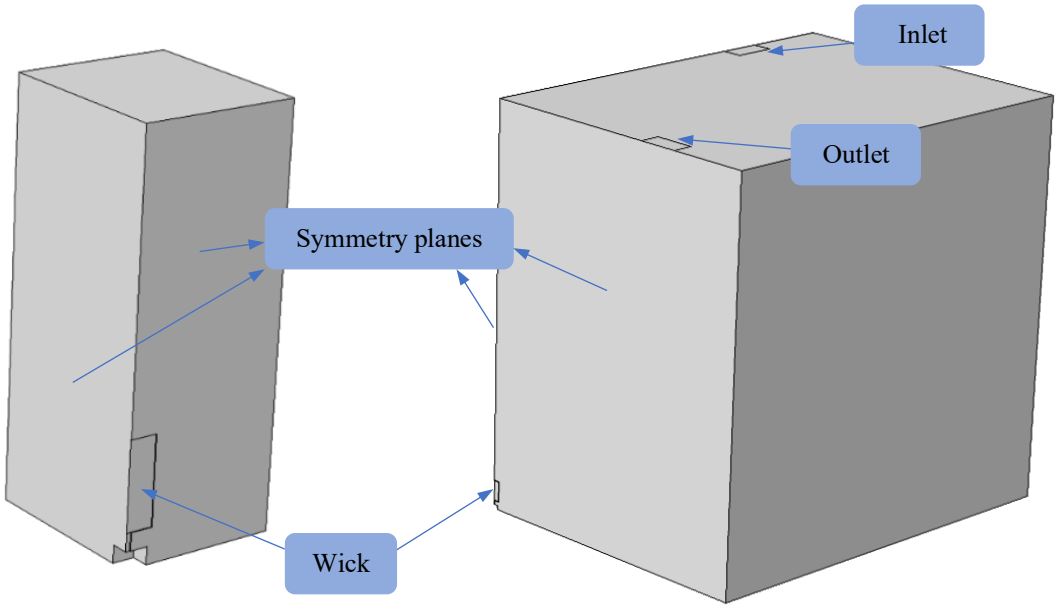

(a) In a chamber (b) In a room

Fig. 20 The 3D geometries of working fluid domain built in COMSOL.

The pressure boundary condition for the outlet is $P_0=0$, and backflow is suppressed so that the outlet pressure is adjusted in order to prevent fluid from entering the domain through the boundary. The velocity boundary condition on the wick is 0. This assumption is

consistent with the assumption of neglecting the inertial in the interface momentum balance equation. For the simulation in a room, the airflow rate at each inlet is at least 0.0625m/s as discussed in Chapter 5. The boundary condition for all the walls is no-penetration and no-slip wall boundary condition. The Robin boundary condition on the wick surface is updated at each timestep with equation (4.4.4),

$$\dot{m} = -D_e \left.\frac{\partial C}{\partial x}\right|_{x=H} = \phi\left(\frac{2\alpha}{2-\alpha}\right)\sqrt{\frac{M_v}{2\pi R_u T_s}}\left[\overline{p}_l - c\big|_{x=H} P_{air}\right].$$

The wicking process is included in the simulation as the 1st stage. The liquid pressure along the vertical direction of the wick is calculated based on equation (4.4.1),

$$\overline{p}_l(z) = P_{atm} - \frac{2\sigma\cos\theta}{r} + \left[\rho_f g - \frac{\mu}{\kappa}\frac{A_0 - 2Hb_0}{2Hb}\frac{dh}{dt}\right]\left(z_T(t) - z\right)$$
$$-\frac{\mu}{\kappa}\frac{1}{\rho_f H}\left\{\left[z_T(t)-z\right]\int_{d_0}^{z}\dot{m}(\xi)\,d\xi + \int_{z}^{z_T(t)}\dot{m}(\xi)\left[z_T(t)-z\right]d\xi\right\}, \quad d_0 \le z \le z_T(t)$$

$z_T(t)$ and $h(t)$ are updated at each timestep using (4.4.2)

$$\phi\frac{dz_T}{dt} + \frac{A_0 - 2Hb_0}{2Hb}\frac{dh}{dt} = -\frac{1}{\rho_f H}\int_{d_0}^{z_T(t)}\dot{m}(\xi)\,d\xi$$

and (4.4.3)

$$\frac{A_0 - 2Hb_0}{2H}\left(\frac{z_T(t) - d_0}{b} + \frac{d_0 - h(t)}{b_0}\right)\frac{dh}{dt}$$
$$= \frac{\kappa}{\mu}\rho_f g\left[z_T(t) - h(t)\right] - \frac{\kappa}{\mu}\frac{2\sigma\cos\theta}{r} - \frac{1}{\rho_f H}\int_{d_0}^{z_T(t)}\dot{m}(\xi)\left[z_T(t) - \xi\right]d\xi$$

at the first timestep. The initial dz_T / dt at the bottom of the wicking pad is calculated based on (4.2.10) $b_0\,\overline{w}\big|_{d_0^-} = b\,\overline{w}\big|_{d_0^+}$, where $\overline{w}\big|_{d_0^-}$, the capillary velocity at the top of the stem is

calculated by the Lucas-Washburn equation. Initial values for h and $\overline{p}_l(z)$ are calculated based on the initial z_T. At the 2nd stage, when the wicking pad is fully soaked with fragrance, z_T is kept constant.

6.3.4 Grid independence study

COMSOL uses the finite element method to compute Multiphysics simulations. To ensure that the error is below some accepted tolerance level, and to save the computational cost at the same time, a mesh refinement study is necessary. It is important to use finer mesh in regions near the evaporation pad and to provide a good transition to regions where larger elements can be used.

With the model in a chamber, a structured mesh is built. The mesh refinement study is imposed based on a stationary study with buoyancy force included in the fluid domain. Assume the wick stays uniformly filled with fragrance, and the walls are kept with 0 concentration. The mesh is refined by 50% three times, which means the grid refinement ratio *r=1.5*. The meshes are shown in Figure 21.

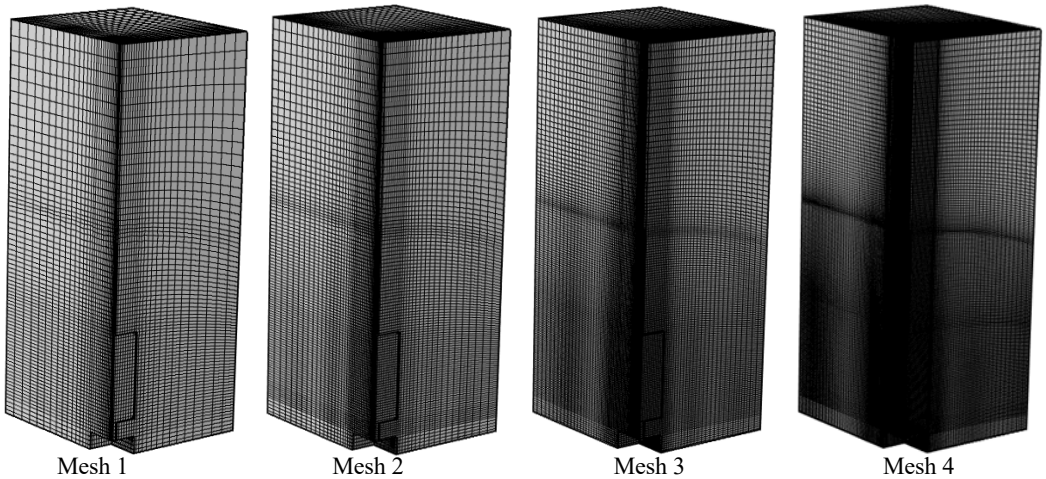

Fig. 21 Mesh for the fluid domain in a chamber.

The normal mass flux over the wick is recorded for each mesh. The data is shown in Figure 22:

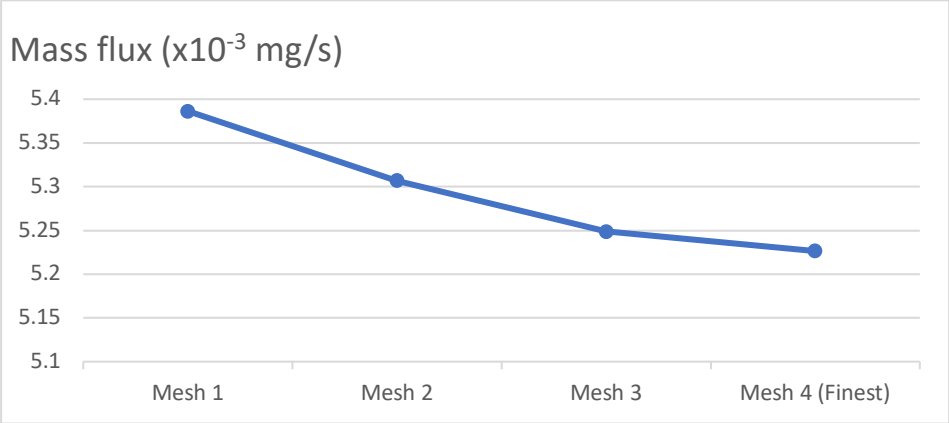

Fig.22 Tracking mass flux for mesh refinement study for the in-chamber model.

GCI method (grid convergence index) is used to determine discretization error and to report grid convergence quality [71]. GCI is a measure of the percentage of the computed values away from the value of the asymptotic numerical value. It indicates how much the solution would change with further refinement of the grid. Thus, a small GCI value indicates that the computation is within the asymptotic range. Since four meshes were built, two separate GCIs are calculated. The order of convergence for each GCI is calculated by

$$p = \frac{\ln\left(\frac{f_i - f_{i+1}}{f_{i+1} - f_{i+2}}\right)}{\ln(r)}, \tag{6.3.12}$$

where f represents the values of obtained mass flux for each mesh. The notation i is the coarsest mesh and $i+2$ is the finest. GCI is calculated by

$$GCI_{i,i+1} = F_{\text{sec}} \frac{|\varepsilon|}{r^p - 1}, \tag{6.3.13}$$

where F_{sec} is the safety factor and the recommended value for three or meshes is 1.25 [72]. $\varepsilon = \frac{f_i - f_{i+1}}{f_i}$ is the relative difference between subsequent solutions. The asymptotic range of convergence is calculated by

$$GCI_{asymptotic} = \frac{GCI_{i+1,i+2}}{GCI_{i,i+1}} r^p. \quad (6.3.14)$$

Table 5 shows the data for the refined meshes and the calculated data for grid convergence index:

Table 5. Tracking Data for Mesh Refinement Study for the In-chamber Model

Mesh	Number of elements	Mass flux ($x10^{-3}$mg/s)	r	p	GCI	$GCI_{asymptotic}$
Mesh 1	57,445	5.3864				
Mesh 2	143,676	5.3069	1.5	0.7692	5.12%	1.0112
Mesh 3	411,666	5.2487	1.5		3.79%	
Mesh 2	143,676	5.3069				
Mesh 3	411,666	5.2487	1.5	2.3659	0.86%	1.0015
Mesh 4	1,242,566	5.2264	1.5		0.33%	

In Table 5, the value of GCI becomes lower for finer mesh, Mesh 3 and Mesh 4 both have the GCI value lower than 1%. The ratio calculated by (6.3.12) provides the check to ensure that the calculated solutions are within the asymptotic range. Mesh 3 is finally chosen considering the computing cost. The mesh consists of 411,666 domain elements.

The same mesh refinement analysis is done with the fluid domain in a room. The mesh is refined 100% each time. A stationary study with buoyancy force included is imposed with each mesh. Assume the wick keeps uniformly filled with fragrance, and the side walls

are kept with 0 concentration. The velocity at the inlet is 0.1m/s. The meshes are shown in Figure 23.

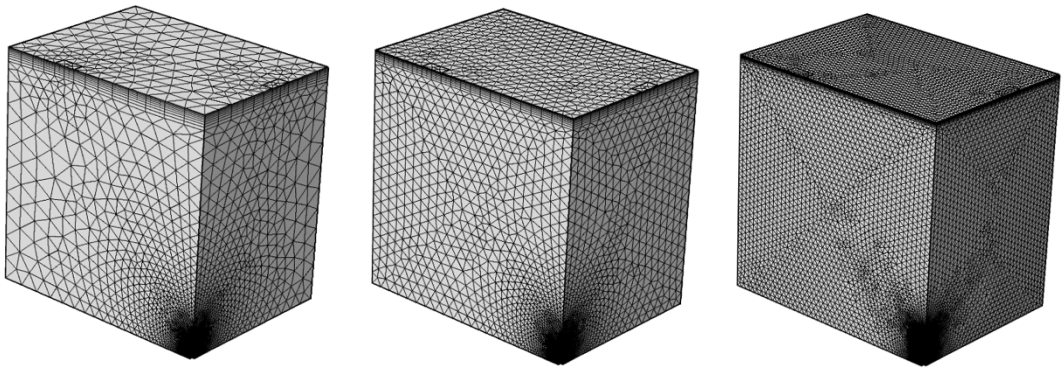

Fig.23 Mesh for the fluid domain in a room

The data for mass flux over the wick for each mesh is shown in Figure 24.

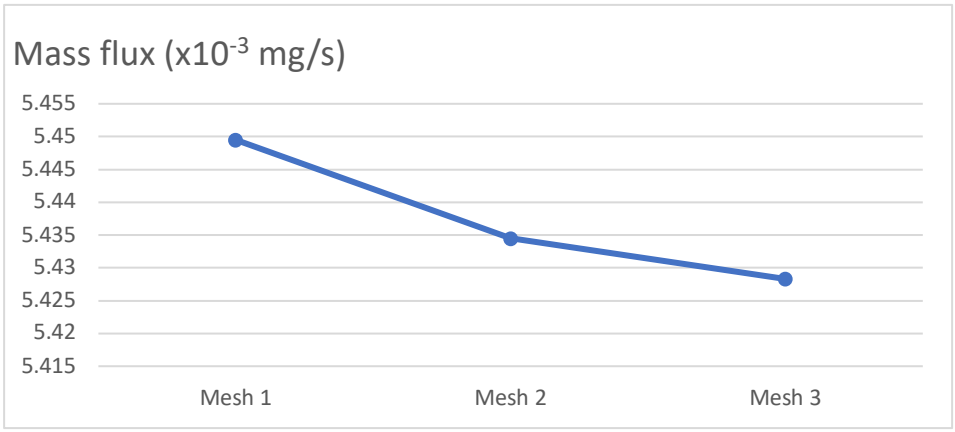

Fig.24 Tracking mass flux for mesh refinement study of the model in a room.

In Table 6, the value of the convergence index is as small as 0.1% for GCI_{23}. The ratio $GCI_{asymptotic}$ is close to 1, which shows that the solutions are within the asymptotic range. Mesh 3 is chosen. The mesh consists of 1,063,046 domain elements.

Table 6. Tracking Data for Mesh Refinement Study for the Model in a Room

Mesh	Number of elements	Mass flux ($x10^{-3}$mg/s)	r	p	GCI	$GCI_{asymptotic}$
Mesh 1	190553	5.4495				
Mesh 2	266084	5.4345	2	1.2746	0.24%	1.008
Mesh 3	1063046	5.4283	2		0.1%	

6.3.5 Numerical simulation

Time-dependent problems in COMSOL are solved with an adaptive time-stepping scheme. The time step size is automatically adjusted to maintain the desired tolerance. In COMSOL, a time step in the BDF time-stepping scheme get accepted if the local truncation error $\left|\bar{e}_k\right| \le Tol_{abs} + Tol_{rel}\left|U^k\right|$, where Tol_{abs} is the absolute tolerance and Tol_{rel} is the relative tolerance, U is the solution of the variable at time t_k. In our simulation, the absolute tolerance is 5×10^{-5} and the relative tolerance is 10^{-4}. In each time step, the pressure and velocity field in the fluid domain are computed, as well as the concentration of the fragrance vapor. The liquid pressure inside the wick, the mass flux along the wick, and the liquid height in the bottle are updated at each time step. A segregated solver is used for each time step. For coupling the pressure-velocity terms, the algebraic multigrid solver (AMG) has been implemented since it always provides robust solutions for large CFD simulations. The discretization is linear. The iterative method of generalized minimal residual (GMRES) is used to solve the momentum and continuity equations. The direct method PARDISO is used to solve the concentration profile as it is the fastest direct solver.

6.4 Numerical solutions and comparison with experiments

As discussed in 6.3.3, the prediction of the wicking process is improved by adding the diffusion and natural convective effect for evaporation on the surfaces of the wicking pad. Most of the parameters used in the simulation are listed in Table 1 and Table 2 in Chapter 2. The vapor density is derived based on the measured vapor pressure using the ideal gas law. The chemical composition in the fragrance is complicated and trade secret. The patent of aqueous perfume oil shows that a typical fragrance used in an air freshener contains at least 70% of water by weight and at least 20% alcohol [73]. In our study, the diffusion coefficient and molecular weight of the fragrance are estimated by assuming the fragrance contains only water and alcohol with the weight ratio of 3:1. Table 7 shows these properties used in our study.

Table 7. More Properties of the Fragrance

Molecular weight (kg/mol)	Mass diffusion coefficient (m^2/s)	Vapor density (kg/m^3)
25	$2x10^{-6}$	0.028

Figure 25 (a) shows the capillary rise started from when the liquid enters the evaporation pad from the stem ($z_T = 0.4cm$) till the pad is fully soaked with the liquid. It matches the result from the experiment well. This also shows that neglecting the 2D effect on the wicking pad by assuming the pressure inside the wicking pad is uniform at any horizontal level is a feasible simplification.

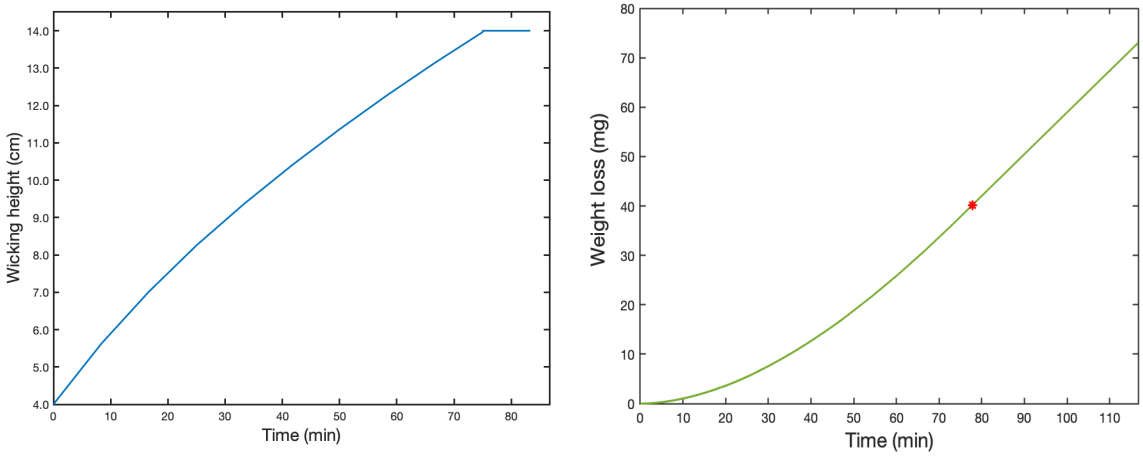

(a) Capillary height (b) Weight loss

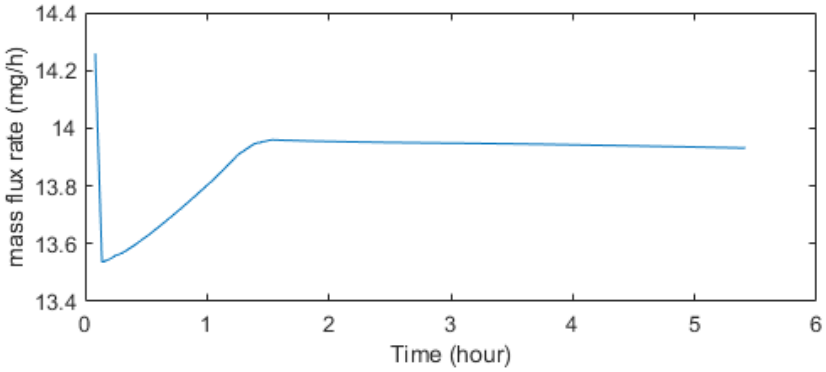

(c) Mass flux rate

Fig. 25 Wicking performance including evaporation and convective effects.

The growth of the weight loss and the variation of the mass flux rate at the first few hours are shown in Figure 25 (b) and (c). The marked point in Figure 25 (b) indicates where the wicking pad gets fully soaked with fragrance. It is observed that the mass flux rate is the highest at the beginning when there's no fragrance in the environment. After the pad gets fully soaked, the evaporation rate decreases slowly with time.

6.4.1 Simulation with the air freshener inside a chamber

Figure 26 shows the comparison of weight loss from 3D numerical simulation with the experimental data, as well as the 1D numerical solution for the model with the air freshener

placed in a chamber for a long time period. With the buoyancy effect taken into account, the 3D simulation result is much closer to the experiment result. It has been illustrated in Chapter 5 that the evaporation rate decreases with time due to the higher concentration of fragrance in the chamber. Figure 26 shows that this phenomenon is more obvious for the numerical result. The weight loss curve from the experiment decays slower than the 3D numerical result. It is because the lid of the chamber is partially open in the experiment, which allows the fragrance vapor to move out, thus the chamber is more difficult to get saturated by fragrance.

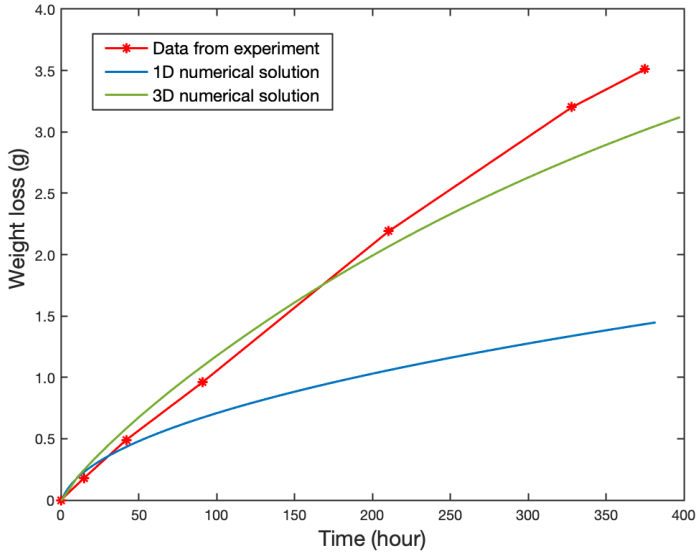

Fig. 26 Comparison of experimental data and numerical results with the freshener placed inside a chamber.

The concentration and the velocity profile with logarithmic arrow length at t=100h in the chamber are shown in Figure 27. The buoyancy effect is observed near the evaporation pad. The concentration profile in Figure 27 (a) shows that at t=100h, the mass fraction of the fragrance vapor remains low in most area of the fluid domain. This indicates that the fresh air remains dominant within the time of interest. Using zero concentration of the

fragrance as reference in the Boussinesq approximation discussed in 6.3.1 is valid. However, if the simulation is run till the chamber is saturated with the fragrance vapor, zero concentration is no longer proper as the reference. The averaged density of the air-fragrance mixture should be used as a reference value.

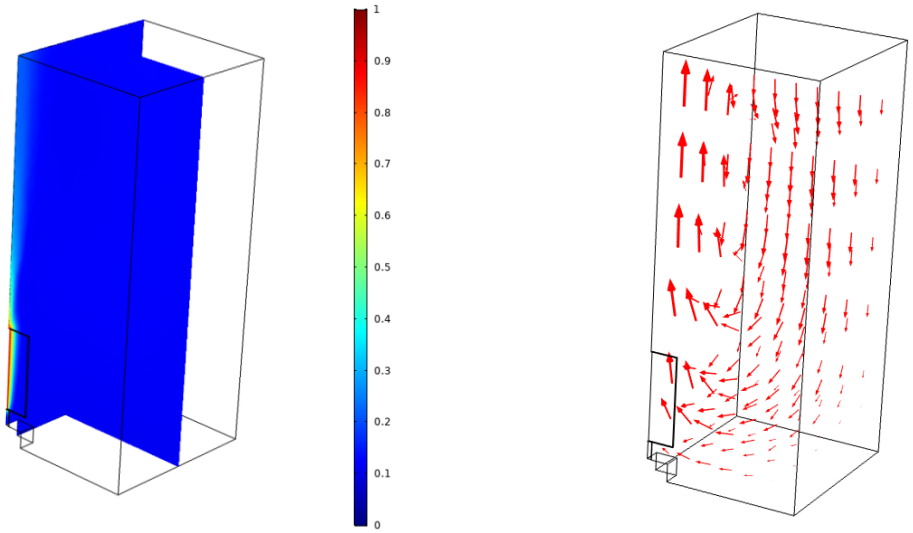

(a) Concentration profile (b) velocity quiver plot

Fig. 27 concentration and the velocity profile at t=100h.

6.4.2 Simulation with the air freshener in a room

Figure 28 shows the results with the air freshener placed in the lab room without a chamber. The weight loss curves from 3D simulations with different airflow conditions are compared with the experimental result. It is observed that with no airflow, the rising rate of the weight loss is the same as the result when the wicking unit is placed in the chamber before the chamber gets saturated. Applying the inlet velocity as 0.0625m/s, the minimum velocity required by ASHRAE standard, the weight loss curve is still far away from the experimental result. A higher inlet velocity is tested and by applying a 0.1m/s velocity,

which still satisfies the recommended ventilation airflow by ASHRAE, the weight loss curve is close to the experimental result.

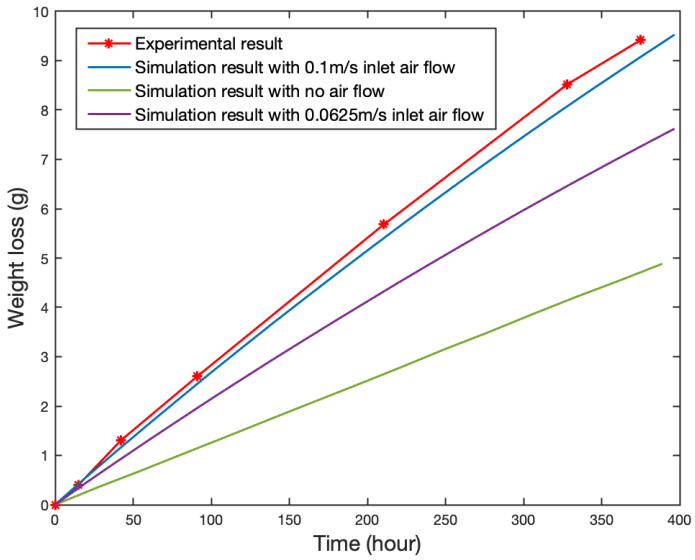

Fig. 28 Comparison of weight loss with the air freshener placed in a room under different airflow conditions.

6.5 Dry-out of the evaporating pad

As the level of liquid inside the container approaches zero, the liquid in the pad starts to dry out. Although this final period is of little interest to the makers of the air fresheners, it is briefly discussed here for completeness.

Combining (4.4.2) and (4.4.3) and take $h \to 0$, it is derived that

$$\phi \frac{dz_T}{dt} = -\frac{\kappa}{\mu}\rho_f g + \frac{\kappa}{\mu z_T(t)}\frac{2\sigma\cos\theta}{r} - \frac{1}{\rho_f H z_T(t)}\int_{d_0}^{z_T(t)} \xi \dot{m}(\xi) d\xi. \tag{6.5.1}$$

The pressure inside the wick is

$$\bar{p}_l(z,t) = P_{atm} - \frac{2\sigma\cos\theta}{r} + \rho_f g\left(z_T(t) - z\right) + \frac{\mu}{\kappa}\phi\frac{dz_T}{dt}\left(z_T(t) - z\right)$$
$$+\frac{\mu}{\kappa}\frac{1}{\rho_f H}\left[\left(z_T(t) - z\right)\int_z^{z_T(t)} \dot{m}(\xi)\,d\xi - \int_z^{z_T(t)} \dot{m}(\xi)\left[z_T(t) - z\right]d\xi\right]. \tag{6.5.2}$$

Take the steady operation pressure $\bar{p}_l(z,0) = P_{atm} - \frac{2\sigma\cos\theta}{r} + \rho_f g\left(d_0 + d - z\right)$ as the initial pressure and update the mass flux by (6.2.4),

$$\dot{m} = \frac{\rho_{vap}\sqrt{D_e}}{\sqrt{\pi}}\frac{\bar{p}}{P_{air}}\frac{1}{\sqrt{t}}.$$

The decaying mass loss rate and the level of the fragrance in the pad are shown below in Figure 29. It's estimated that the wicking pad will dry out in 40 minutes after the bottle is empty.

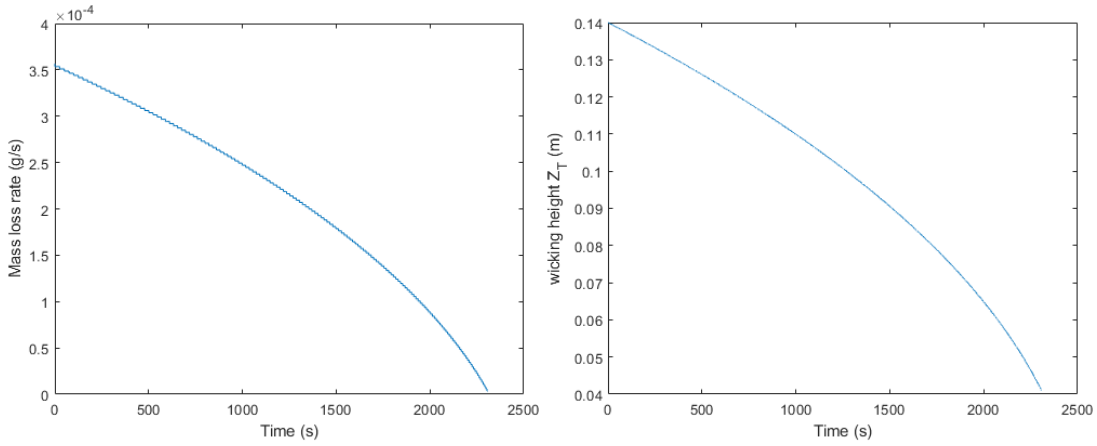

(a) Mass loss rate (b) Wicking height

Fig. 29 The decaying process for the dry-out period

CHAPTER 7

EVAPORATION OF GEL-BASED AIR FRESHENER

7.1 Introduction

Gel-based air freshener is another type of passive air freshener in the market. A gel is a colloidal system in which a nanostructured network of interconnected particles spans the volume of a liquid medium. The capillary forces exerted by the liquid are strong since the pore size of a gel is at a nanometer scale. Shrinking will occur when the liquid evaporates from the surface of the gel. As molecules of liquid escape into the air, the surrounding liquid molecules are pulled together by capillary action and tug on the framework of the gel. It results in the collapse of the framework of the gel, forming a dense structure [74]. The evaporation rate of gel is affected by the atmospheric conditions, the structure of the porous medium, and transport properties. The book of Brinker & Scherer [75] illustrates that the drying process of the gel contains several stages as shown in Figure 30. At the first stage, each volume of evaporated solvent is lost by the gel. The body shrinks by the same amount of volume as the liquid evaporates. The liquid-vapor interface remains at the exterior surface of the body. The gel network is drawn into the liquid by capillary. At the second stage, the gel becomes too stiff to shrink, air invades the pores. Evaporation continues at the surface with a falling rate, the liquid escapes only by diffusion of its vapor to the surface.

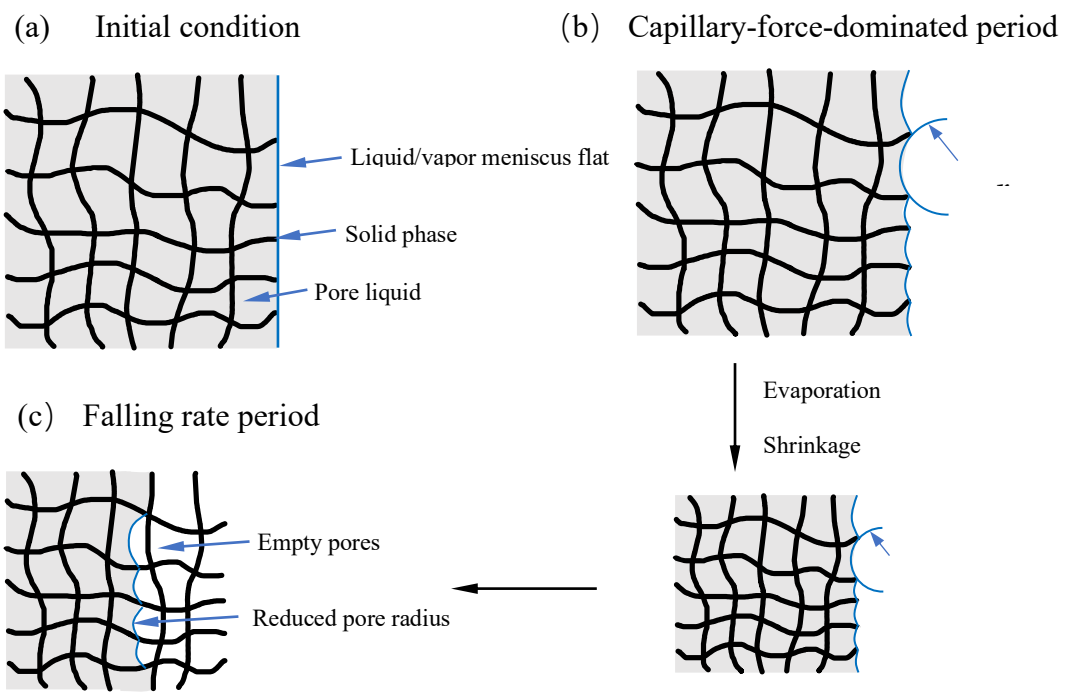

Fig. 30 Schematic illustration of stages of drying for gel [75]

The stages of drying with porous materials were first proposed in Sherwood's work [76]. They include the capillary-flow-dominated stage 1 with little change in the rate of evaporation per unit area and the diffusion-dominated stage 2 with a lower evaporation rate [77]. During stage 1, water evaporates from the surface of a saturated porous medium and it is replaced by mass flow from the invading drying front, which is the interface between the saturated and transition zones [78]. Dwivedi's experimental data indicates that during the first stage, the evaporation rate of water from the alumina gel is nearly constant and close to that from a dish of water [79]. As illustrated in Figure 30, the network is initially compliant, capillary force acts as if the network was submitted to isostatic compression that causes it to contract into the liquid. New bonds are forming with the network of the gel as drying proceed, thus the porosity decreases, the capillary tension in the liquid rises,

and the radius of the meniscus decreases continuously. Factors other than capillary force are discussed by many researchers. Wayner et al. [80] discussed the adsorption force that enhanced evaporation rate by driving a film of liquid on the surface and draw flow to compensate for evaporation. Electrostatic repulsion and other disjoining forces are discussed by Macey [81] and Spitzer [82], which are significant only for clay gels. Brinker & Scherer [75] claim that these effects increase the resistance of the network to compression and the viscosity near a solid-liquid interface. Schlünder [83] discussed the drying performance on a partially wetted surface and states that the drying rate during the constant rate period is controlled by three length scales: the length of the sample, the pore size, and the length of the mean free path of the gas molecules. An expression for evaporation rate depending on 2D surface water content is obtained. The relative mass transfer coefficient, as the ratio of the mass transfer from a partially wet area to that from a free water surface, is

$$\frac{\dot{m}}{\dot{m}_0} = \frac{1}{1+\frac{2}{\pi}\frac{r}{\delta_m}\sqrt{\frac{\pi}{4\varphi_w}}\left[\sqrt{\frac{\pi}{4\varphi_w}}-1\right]}, \tag{7.1.1}$$

where r is the radius of wet patches, δ_m is the thickness of the mass boundary layer, φ_w is the surface water content. The expression is valid only for the range of $\varphi_w \le \pi/4$ due to the square shape of the unit cell assumed in the derivation [84]. Equation (7.1.1) was also used to explain the end of the constant rate period since the evaporation rate decreases as φ_w is small enough [85]. Schlünder's formula (7.1.1) provides a reasonable drying rate but is limited to when the surface is spatially periodic with uniform pore size. The structural

change of the pores and the convective effect are neglected [86]. Another approach studying the evaporation in a porous medium by simulations on pore networks is proposed by Laurindo and Prat [87] [88]. The simulator is based on an invasion algorithm combining elements of the invasion percolation algorithm with the computation of the vapor flux at each elementary liquid-gas interface [88]. Percolation theory is often used to analyze multiphase immiscible displacements governed by capillary effects on networks [89]. The mass flux at an elementary liquid-gas interface within the network is computed as

$$\dot{m} = d^2 \rho \frac{c_{eq} - c_{i,j}}{\alpha l}, \tag{7.1.2}$$

where d is the width of the bond between pores, ρ is the density of the gas phase, αl is the distance between the elementary liquid-gas interface and the center of the adjacent gas pore. c_{eq} and $c_{i,j}$ are the concentration of the liquid-vapor at equilibrium status and at the node i,j of the network. The agreement with experiments was only qualitative, however. The constant rate is captured with their 3D network simulation [90]. Yiotis et al. [91] simulate the drying process with a 3D pore-network model that accounts for capillarity and buoyancy at the interface and shows that the constant drying rate is maintained while liquid connections between the evaporating surface and drying front are maintained. Lehmann et al. [78] compared the roles of gravity, capillary, and viscous dissipation, and derived characteristic lengths from pore size distribution that determine the maximum drying front depth at the end of stage 1. Their approach enables a prediction on the duration of the constant rate period.

As shown in Figure 30 (c), the shrinkage stops as the capillary forces in the liquid cannot overcome the stiffening of the network, and the meniscus recedes into the pores [75]. The capillary stress at the critical point can be written as

$$P_R = \sigma_{LV} \cos\theta \left(\frac{S\rho_s}{1-\rho_{rel}} \right), \tag{7.1.3}$$

where σ_{LV} is the liquid-vapor surface tension, θ is the contact angle, S is the specific surface area of the drained network, ρ_s is the bulk density of the solid network, ρ_{rel} is the relative density. The lower evaporation rate in stage 2 is dominated by vapor diffusion. Mosthaf et al. [77] studied the influence of hydraulic properties of the porous medium on the transition from stage 1 to stage 2 by coupling the free flow and porous medium flow. They presented a model to predict the evaporation behavior during the transition. However, the comparison with experimental results shows the limitation of the model. Shokri et al. [92] studied the effects of partial wettability caused suppression of evaporation by a pore-scale model. Their experimental results indicate that the primary effect concerning evaporation from mixed-wettability media is due to diminishing capillary driving forces. Shokri et al. [93] observed the formation of the vaporization plane at stage 2, when the liquid menisci recede into the porous medium. They estimated the drying rate during stage 2 according to Fick's law as:

$$J = \frac{\varphi_a^{2.5}}{\phi} D_e \frac{\rho_{sat} - \rho_\infty}{L_{dried}}, \tag{7.1.4}$$

where φ_a is the volumetric air content, ϕ is the porosity. It is assumed that the volumetric air content is above the receding vaporization plane. ρ_{sat} and ρ_∞ are the saturated water

vapor density at the receding vaporization plane and the water vapor density above the plane. D_e is the vapor diffusion coefficient in free air. L_{dried} is the thickness of the dry surface layer, which is measured from the experiment. The predicted evaporation rate matches the measured data from experiments well.

Evaporation performances at different stages are studied in all of the above research. Some of them provided the expressions for evaporation rate. However, they are estimated either based on strict experimental measurements [93] or by the empirical correlation equation [83]. The simulations based on the assumption of percolation patterns predict the local evaporation performance well in pore-scale. However, the computational cost is too high and the shrinkage of the solid network of the gel is ignored. To better predict the entire global evaporation performance of a gel-based air freshener, the atmospheric conditions, the structure of the porous medium, and transport properties that influence the evaporation rate of gel are all taken into consideration in our analysis.

7.2 Experiment on gel-based air freshener

Hankel USA in Scottsdale, Arizona, has performed experiments on their carrageenan gel air freshener shown in Figure 31. The samples comprise about 5% by weight of fragrance, a 10% by weight of carrageenan together with nonionic cellulose derivative, and water. The essential fragrance oil blends are diluted with solvents of ethanol [94]. The cylindrical gel sample is originally 4.2cm high with a radius of 2.2cm. The initial mass and volume are 64.3g and 63.86cm^3. The initial total surface area is 73.26cm^2. The other sample is modeled as a perfect hemisphere with an initial contact angle $\theta = 90^o$ and radius of 2.92cm. The initial mass and volume are 45.8g and 45.23cm^3. The initial surface area is

48.85cm^2. Both samples are placed in an empty lab on flat smooth substrates separately with no wick applied. The liquid can evaporate freely to the ambient air at the same time avoid being affected by airflow. The temperature in the lab is kept constant at 77^{o}F.

Fig. 31 The initial condition of the gel samples

The weights of the units are measured every 8 hours. Figure 32 shows how the shape of the gel samples changed with time. It is observed from Figure 32 (a) that the volatile compound near the top edge of the cylindrical gel evaporates faster. The top edge becomes rounded quickly because the local evaporation rate is proportional to the local curvature of the meniscus. Hu & Larson [95] studied the nonuniform evaporation flux distribution at different contact angles and claims that the nonuniformity in evaporation rate drives an outward Marangoni flow. From Figure 32 (b), it is observed that as the gel evaporates, the surface of the spherical surface descends. The contact radius of the spherical gel sample reduces at a slower rate than the contact angle.

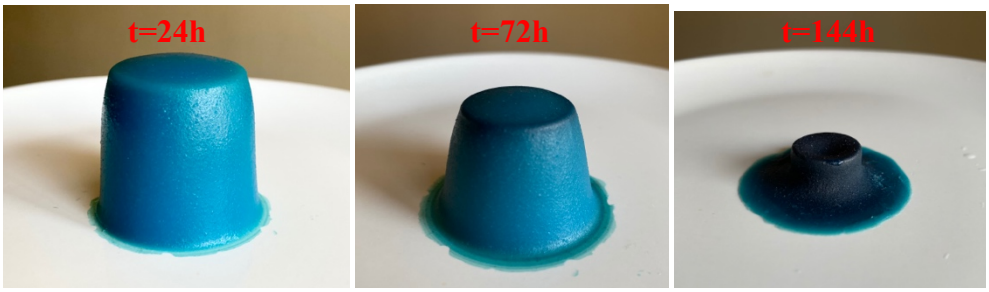

(a) Cylindrical sample

(b) Hemispherical sample

Fig. 32 The evaporation and shrinkage of gel samples with time.

The weights of the gel samples are recorded and plotted in Figure 33. For each sample, weight loses at a constant rate at first (the slope of the weight curve is nearly constant), indicative of a constant global evaporation rate. The slope reduces slowly with time as the area of the evaporation surface is reduced. The initial evaporation rate for the cylindrical gel is higher than the hemispherical gel due to its larger evaporation surface area.

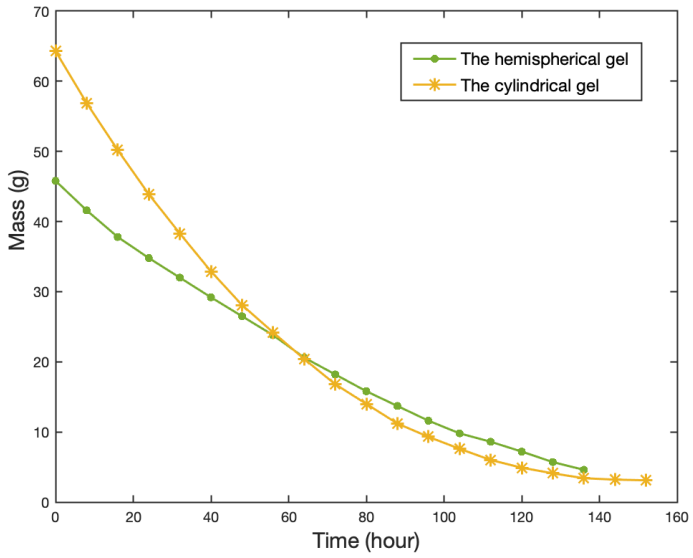

Fig. 33 The total weight of the gel samples measured from experiments at different time

7.3 Sessile drop model

A sessile drop of a pure substance is used as our first model to estimate the evaporation performance of the gel-based air freshener. Convection of the ambient air is ignored. The evaporation of a sessile drop is studied by many researchers. Birdi and Winter [96] reported that the rate of evaporation of sessile drops of water on a glass surface remains constant by measuring the weight change of the water droplet. Shanahan and Bourges [97] [98] examined the evaporation behavior of sessile drop of water and *n*-decane on different materials of substrates and observed that the evaporation occurs in several distinct stages as shown in Figure 34.

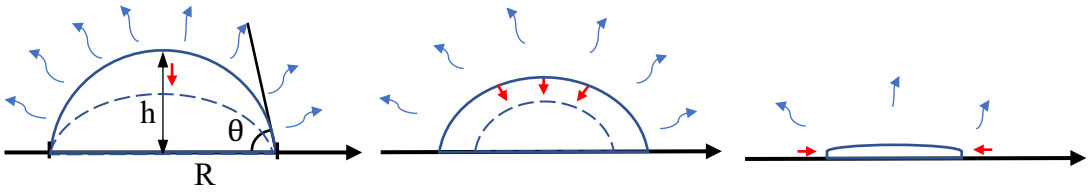

(a) Stage I (b) Stage II (c) Stage III

Fig. 34 Schematic representation of sessile drop evolution during evaporation [97]

In the first stage, the contact diameter remained constant. The drop in height h and contact angle θ diminished rapidly. The drop in height and contact diameter diminished roughly in proportion in the second stage. In the final stage, the drop disappears in an irregular fashion. They proposed an evaporation model by taking the concentration gradient of a droplet in the shape of a spherical cap and ignored the non-uniform distribution along the droplet surface.

Rowan et al. [99] analyzed the evaporation rate using a diffusion model and a spherical cap geometry. Their model fits experimental results for microdroplets with large initial contact angles. Erbil and Meric [100] built the vapor diffusion model of a droplet based on a three-parameter ellipsoidal cap. A better agreement with the experiments has been obtained compared to the spherical model. They [101] developed another model with pseudospherical cap geometry by introducing another parameter α, the adjustable flatness parameter to better evaluate the surface area and volume of the drop body. They argued that the results fit better with experimental results. Hu and Larson [102] developed a new model to evaluate the vapor concentration and evaporation flux of a droplet with the shape of a spherical cap on a smooth substrate using the finite element method. They observed that the phase where the contact line remains pinned as contact angle decreases takes up 90-95% of the total drying time Their experimental measurements confirms that the droplet evaporation is a quasi-steady-state process and claims this is true whenever the vapor phase has a density much smaller than that of the liquid. The results predicted by the finite element method agree well with experimental results and are confirmed by the analytical

solution by Lebedev [103] for an initial contact angle θ between 0 and $\pi/2$ in radians. They claimed that the finite element method remains accurate for a very wide range of conditions including when the droplet is not a spherical cap because of the gravity sag and when the temperature is not uniform inside the droplet. The approximate evaporation rate expression of a sessile droplet with a pinned contact line is derived by curve fitting using a parabola with respect to the contact angle as

$$\dot{M} = -\pi R D_e \left(1 - H_a\right) \rho_{vap} \left(0.27\theta^2 + 1.3\right), \tag{7.3.1}$$

where R is the contact radius, D_e is the diffusion coefficient. H_a is the relative humidity of the ambient air. ρ_{vap} is the saturated water vapor density, θ is the contact angle.

With the support of the polymer structure, a gel in the shape of a spherical cap can be analogous to a droplet with gravitational sag neglected. It is observed from our experiment that the shrinking of the contact radius is much slower than the decrease of the contact angle. Thus, the sessile drop model with the contact line pinned can be used to predict the drying performance of the gel as shown in Figure 34. To keep the problem tractable, the following additional assumptions will be made: (i) the water is at a uniform saturated state on the spherical cap surface; (ii) The air is stagnant, thus only diffusion is considered; (iii) The shape of the gel changes slowly compared to the time scale for vapor diffusion in the air (quasi-steady assumption).

As the liquid evaporates, the contact radius R is kept as a constant, and the contact angle decreases with time. The relationship between the mass of the gel and the contact angle for a spherical cap at any time is expressed as

$$M(t) = \rho_f \pi R^3 \frac{2 - 3\cos\theta + \cos^3\theta}{3\sin^3\theta}, \tag{7.3.2}$$

where ρ_f is the density of the liquid, θ is the contact angle. For $0 < \theta \le \pi/2$, θ^2 can be fitted well as a function of a dimensionless parameter $\Lambda = \frac{M(t)}{\rho_f \pi R^3}$ by a 4th degree polynomial

$$\theta^2 = 18.17\Lambda^4 - 33.32\Lambda^3 + 19.95\Lambda^2 - 0.15\Lambda. \tag{7.3.3}$$

Coupling (7.3.3) with (7.3.1), the weight change of the gel with time is derived. The contact radius of the gel sample is 2.92cm. The initial weight is 45.8g. The relative humidity for the experimental environment is assumed to be 20%, which is the average humidity in April in Scottsdale, Arizona. The diffusion coefficient of water vapor in the air at room temperature 77°F is used as the diffusion coefficient for the evaporating fluid in our calculation, which is 2.5×10^{-5} m^2/s. The densities of the evaporating liquid and vapor are calculated by assuming the liquid phase of the gel is composed of 5% of fragrance and 85% of water by the total weight [94]. Since the fragrance components are diluted in ethanol in our product, the properties of ethanol are used as the properties of the fragrance components. At room temperature 77°F, the density of the liquid mixture is calculated based on the mole fraction of water and ethanol. The physical properties of the liquid phase in the gel sample are listed in Table 8.

The vapor density is calculated from saturation vapor pressure of the mixture by the ideal gas law. The actual vapor density is higher because the volatile fragrance components are always with higher vapor pressure [104].

Table 8. The Physical Properties of the Gel Sample

Components of the gel	Molecular weight M_w[mol/g]	Liquid density ρ_f[kg/m^3]	Vapor density ρ_v[kg/m^3]	Diffusion coefficient D_e [m^2/s]
85 wt.% water 5 wt.% fragrance 10 wt.% carrageenan	18.63	985.36	0.025	2.5x10^{-5}

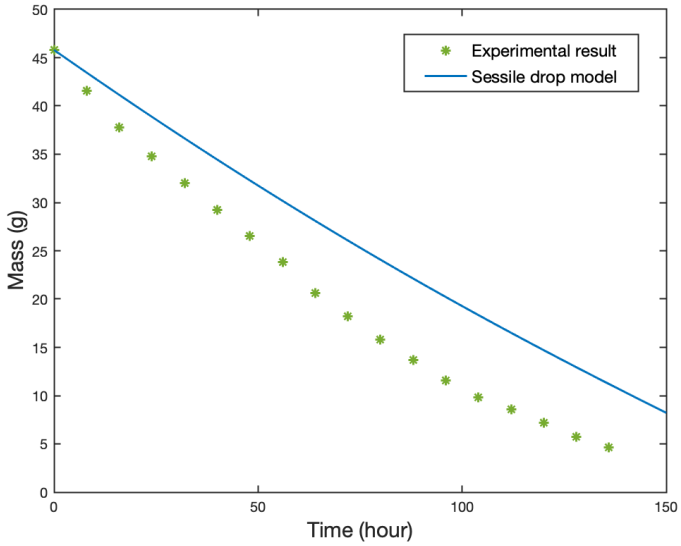

Fig. 35 The mass change of the gel predicted by the sessile drop model compared with experimental results

Figure 35 shows that the mass decline predicted by the sessile drop model performs nearly at constant rates. The evaporation rate predicted is lower than the experimental result as the slope of the mass decline curve is lower than the slope of the experimental mass loss curve. The sessile drop model is a simple preliminary tool to estimate the weight loss performance and life span for the hemispheric sample. The lack of accuracy is due to the many assumptions involved, in particular that the contact line of the gel is pinned.

7.4 Mass diffusion coupled with the evaporation model

The sessile drop model is a model based on a pure substance. In this section, a simple scheme to estimate the performance of a gel-based air freshener is introduced using the evaporation model discussed for the paper-like fibrous material in Chapter 3.

The polymer network structure occupies 10 % of the total weight and the weight of the solid phase is kept as a constant. To simplify the problem, the pore network of the gel is constructed as spherical pores connected by cylindrical tubes with the same radius. As the liquid phase evaporates, the polymer structure shrinks with the number of pores and cylindrical tubes remain the same. As introduced in Chapter 3, the boundary condition at the surface of the porous media is obtained by combining the kinetic theory at the interface and diffusive flux of mass fraction

$$\dot{m} = \phi(t)\left(\frac{2\alpha}{2-\alpha}\right)\sqrt{\frac{M_w}{2\pi R_u T_s}}\left[p_l - c_s P_{air}\right] = -D_e \rho_{vap} \nabla c\big|_{surface}, \tag{7.4.1}$$

where ϕ is the porosity of the gel structure and is a function of time. As the liquid in the gel evaporates, the solid network frame shrinks, the size of the pores decreases, and the porosity changes as well. α is the accommodation coefficient, M_w is the molecular weight of the evaporating liquid, R_u is the gas constant, T_s is the temperature at the surface of the gel. p_l is the liquid pressure at the liquid-air interface, c_s is the mole fraction of the evaporating liquid vapor at the surface, P_{air} is the atmospheric air pressure. D_e is the diffusion coefficient of the liquid, ρ_{vap} is the vapor density. For our gel model, the viscous stress and the inertia term are negligible compared to the capillary effect, the liquid

pressure at the interface can be estimated by subtracting the capillary pressure from the air pressure P_{air}:

$$P_l = P_{air} - \frac{2\sigma\cos\theta_c}{r_p}. \tag{7.4.2}$$

The second term in (7.4.2) is the capillary pressure, where σ is the surface tension, θ_c is the contact angle of the liquid, r_p is the pore radius of the gel structure.

7.4.1 The hemispherical gel sample

To study the evaporation performance of the gel in hemispherical shape, we consider the vapor transport outside the gel with the simplest model where only diffusive transport from the surface of the hemispherical gel sample along the radial direction is included. The spherical diffusion equation is

$$\frac{\partial c}{\partial t} = \frac{D_e}{r^2}\frac{\partial}{\partial r}\left(r^2\frac{\partial c}{\partial r}\right), R_{gel} \le r < R_{wall}, t \ge 0 \tag{7.4.3}$$

where c is the mass fraction of the evaporating fluid, r is the radial distance to the center of the hemispheric gel. In our calculation, the boundaries and the fluid domain are assumed to be fixed for simplicity, which means the radius of the hemispherical gel R_{gel} is assumed to be constant. This is in essence a quasi-steady assumption, justified for a slow evaporation process.

The boundary condition at the surface of the gel $r = R_{gel}$ is defined as

$$\phi(t)\left(\frac{2\alpha}{2-\alpha}\right)\sqrt{\frac{M_w}{2\pi R_u T_s}}\left[P_{air} - \frac{2\sigma\cos\theta_c}{r_p} - c_{r=R_{gel}}P_{air}\right] = -D_e\rho_{vap}\left.\frac{\partial c}{\partial r}\right|_{r=R_{gel}}. \tag{7.4.4}$$

In the experiment, the sample is placed in an empty lab. In our simulation, it is assumed

that the outer boundary is in hemispheric shape with a radius of 5m and Dirichlet boundary condition, which is much larger than the lab and has 0 concentration of the evaporating fluid. The fluid domain is shown in Figure 36.

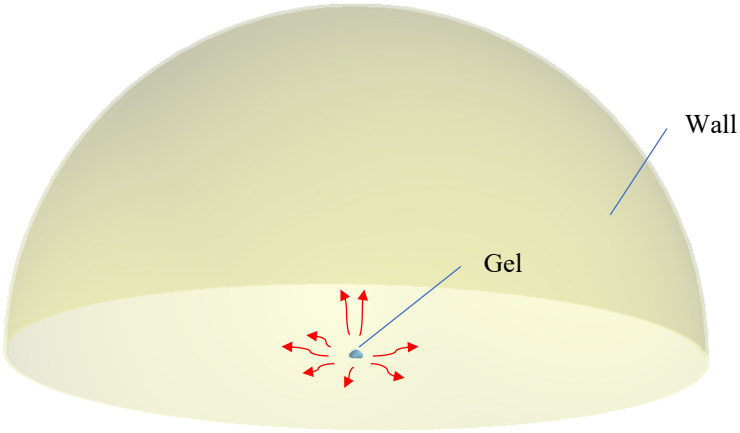

Fig. 36 The sketch of the fluid domain of the diffusion performance with the hemispherical gel sample.

The initial condition for the diffusion domain is $c(r,0)=0$. The backward time central space implicit method is used to solve the diffusion equation. Nonuniform mesh is built with m grid points along the radial direction. The grid size is smaller near the surface of the gel. The stretch ratio is constant and set as 1.005. The grid size for each cell is Δr_i, and the radial distance to the center of the hemisphere at each grid point is r_i. The time step is Δt. The matrix equation used to solve the concentration of each grid point at each time step c_i^{n+1} is:

$$\begin{bmatrix} -1-\frac{2\gamma_1}{\Delta r_1}+\left(\frac{\Delta r_1}{r_1}-1\right)2\gamma_1\beta\cdot P_{air} & \frac{2\gamma_1}{\Delta r_1} & & & \\ 2\gamma_2\left(\frac{1}{\Delta r_1}-\frac{1}{r_2}\right) & -2\gamma_2\left(\frac{1}{\Delta r_1}+\frac{1}{\Delta r_2}\right)-1 & 2\gamma_2\left(\frac{1}{\Delta r_2}+\frac{1}{r_2}\right) & & \\ & \ddots & & & \\ & & 2\gamma_{m-1}\left(\frac{1}{\Delta r_{m-2}}-\frac{1}{r_{m-1}}\right) & -2\gamma_{m-1}\left(\frac{1}{\Delta r_{m-2}}+\frac{1}{\Delta r_{m-1}}\right)-1 & 2\gamma_{m-1}\left(\frac{1}{\Delta r_{m-1}}+\frac{1}{r_{m-1}}\right) \\ & & & 0 & 1 \end{bmatrix} \begin{bmatrix} c_1^{n+1} \\ c_2^{n+1} \\ \vdots \\ c_{m-1}^{n+1} \\ c_m^{n+1} \end{bmatrix} = \begin{bmatrix} -c_1^n+2\gamma_1\left(\frac{\Delta r_1}{r_1}-1\right)\beta\cdot P_l \\ -c_2^n \\ \vdots \\ -c_{m-1}^n \\ 0 \end{bmatrix}$$

(7.4.5)

where $\gamma_i = \dfrac{D_e \Delta t}{\Delta r_i + \Delta r_{i-1}}$ for $i \geq 2$, $\gamma_1 = \dfrac{D_e \Delta t}{\Delta r_1}$, $\beta = \dfrac{1}{D_e \rho_{vap}} \phi(t) \left(\dfrac{2\alpha}{2-\alpha} \right) \sqrt{\dfrac{M_w}{2\pi R_u T_s}}$. P_l is calculated by the equation (7.4.2). The parameters of mass diffusivity and vapor density used are introduced in 7.3. $D_e = 2.5 \times 10^{-5} \mathrm{m}^2/\mathrm{s}$, $\rho_{vap} = 0.025 \mathrm{kg/m}^3$. To calculate the capillary force in (7.4.2), the properties of water are used. The liquid-vapor surface tension is $\sigma = 72 \mathrm{mN/m}$. The contact angle is assumed to be constant and equal to 52° based on the experiments measured using a modified Wilhelmy plate technique on silica gels by Stein et al. [105]. The initial radius of the pores is assumed to be $50 \mu\mathrm{m}$ based on the observation by Sharma et al. [106] that large and interconnected pores of carrageenan-gelatin gel were in the range of 60-100μm diameter. The weight loss of the gel air freshener is entirely due to the evaporation of the fluid trapped within the solid frame. The porosity of the gel at any time can be calculated once the total mass is measured:

$$\phi(t) = \frac{V_f(t)}{V_s + V_f(t)} = \frac{\phi_0 V_0 - M_{evp}(t)/\rho_f}{V_0 - M_{evp}(t)/\rho_f}, \tag{7.4.6}$$

where V_0 is the initial gel volume, V_f is the volume of the liquid phase, and the subscript *s* represents the solid phase. ϕ_0 is the initial porosity and is calculated by measuring the

initial volume of the gel and the volume of the dry gel from the experiment. $M_{evp}(t)$ is the total evaporated mass accumulated within time *t*. Assume the pores are tightly connected cylindrical pores [107] uniformly distributed in the gel, the number of the pores is *N*. To trace the variation of the mean radius of the pores with time, it is assumed that the surface porosity is the same as the bulk porosity, and the area of the solid network frame on the surface of the gel is A_s. the porosity of the gel can be calculated by

$$\phi(t) = \frac{\pi r_p^2(t) N}{\pi r_p^2(t) N + A_s}. \tag{7.4.7}$$

Assume the number of the pores and the area of the solid structure on the surface of the gel are kept the same during the shrinking process. The time-dependent mean pore radius can be derived by the relation below when the initial value $r_{p,0}$ is given,

$$\frac{r_p^2(t)}{r_{p,0}^2} = \frac{\phi(t)(1-\phi_0)}{\phi_0(1-\phi(t))}. \tag{7.4.8}$$

The total evaporating area at any time is then derived using

$$\frac{A_{evap}(t)}{A_{evap,0}} = \frac{r_p^2(t)}{r_{p,0}^2}, \tag{7.4.9}$$

where the initial evaporating area is calculated by $A_{evap,0} = \phi_0 2\pi R_{gel}$. By solving the diffusion equation numerically, the mass loss rate for each time step can be derived by

$$\dot{M}(t) = \phi(t)\left(\frac{2\alpha}{2-\alpha}\right)\sqrt{\frac{M_w}{2\pi R_u T_s}}\left[P_{air} - \frac{2\sigma\cos\theta_c}{r_p(t)} - c_1 P_{air}\right] A_{evap}(t). \tag{7.4.10}$$

Mesh refinement analysis is performed by refining the grid size twice. With the size for the smallest cell next to the boundary of the gel reduced 100% each time and the stretch ratio constant, the three meshes are approximately constructed with a constant refinement ratio of 2. The evaporation mass flux at the last time step $t = 150h$ is tracked for each mesh. Table 9 shows the collected mass flux data for all the meshes and the calculated data for the grid convergence index.

Table 9. Mesh Refinement Data for the Hemispherical Gel Model

Mesh	Grid size of Δr_1 (m)	Mass flux ($x10^{-3}mg/m^2s$)	r	p	GCI	$GCI_{asymptotic}$
Mesh 1	0.002	22.965				
Mesh 2	0.001	22.886	2	1.98	0.15%	0.976
Mesh 3	0.0005	22.866	2		0.037%	

The value of GCI_{23} is as small as 0.037%. The ratio $GCI_{asymptotic}$ is close to 1, which shows that the solutions are within the asymptotic range. The number of grid points is 925 for Mesh 3.

Figure 37 shows the comparison of the mass loss curve predicted by the evaporation model with kinetic theory and the sessile drop model with the experimental data. The curve predicted by the evaporation model with kinetic theory matches the experimental result better. The evaporation model predicts the evaporation rate well for the first 50 hours. However, the deviation between the predicted result and experimental data grows with time. Neglecting the convection effect in the simulation is one of the reasons for the deviation.

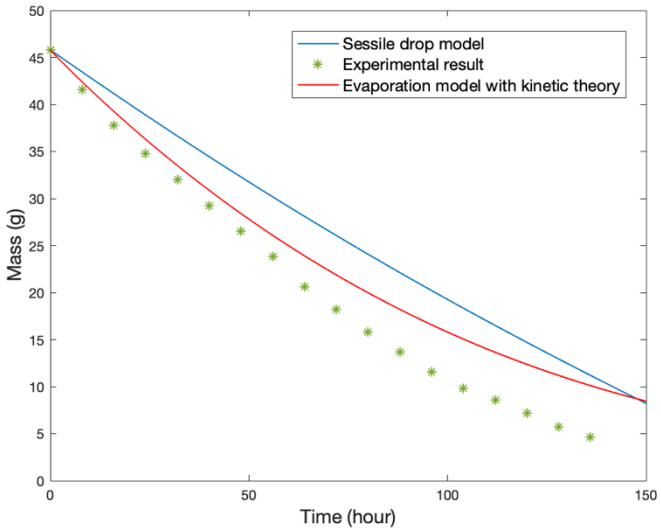

Fig. 37 The mass change of the gel predicted by two theoretical models compared with experimental result

7.4.2 The cylindrical gel sample

A 3D simulation is performed with the cylindrical sample using the commercial software COMSOL Multiphysics. The gel is placed in the center of a closed space with dimensions of 2mx2mx1m. Assuming the air is stagnant and only diffusion is considered. The fluid domain is shown in Figure 38. As it is an axisymmetric flow field, symmetric boundaries are used in the 3D simulation to reduce 75% of computing cost.

The diffusion equation is

$$\frac{\partial c}{\partial t} = D_e \nabla^2 c, \tag{7.4.11}$$

where c is the mass fraction, D_e is the diffusion coefficient of the evaporating liquid in the air.

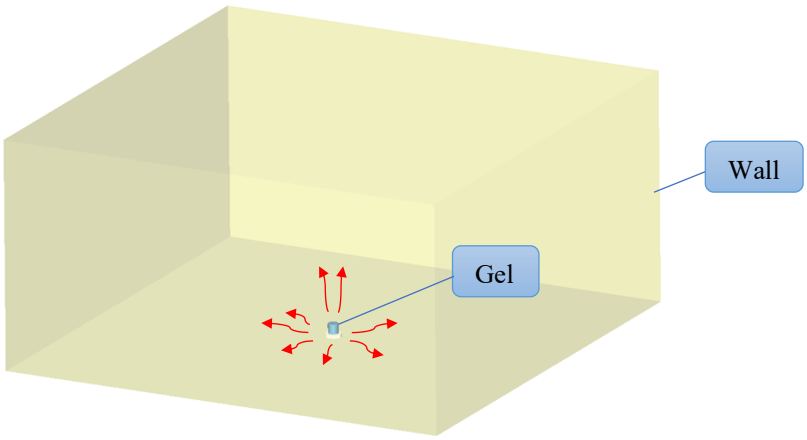

Fig. 38 The fluid domain of the diffusion performance with the cylindrical gel sample.

The same initial condition and boundary conditions as the hemispherical model introduced in Section 7.4.1 are applied. The kinetic theory at the interface is used for both the top surface and the side surface of the gel:

$$\phi(t)\left(\frac{2\alpha}{2-\alpha}\right)\sqrt{\frac{M_w}{2\pi R_u T_s}}\left[P_{air}-\frac{2\sigma\cos\theta_c}{r_p}-c_s P_{air}\right]=-D_e\rho_{vap}\nabla c\big|_{surface}. \qquad (7.4.12)$$

We assume that the physical properties are kept the same for the gel samples in different shapes, thus, the parameters such as diffusion coefficient, vapor density, liquid-vapor surface tension, contact angle, initial pore radius are used the same as the hemispherical model introduced in Section 7.4.1. Structured mesh is constructed in the fluid domain.

A Mesh refinement study is performed by reducing the grid size by 100% twice and running a steady-state simulation for each mesh. The mole fraction of the evaporating liquid is 1 on the surface of the gel and 0 at the boundary walls. The data of the global mass evaporation rate of the entire gel sample are collected for each mesh. The order of convergence and GCI index is calculated and displayed in Table 10.

Table 10. Mesh Refinement Data for the Cylindrical Gel Model

Mesh	Grid size of Δr_1 (m)	Mass loss rate (x10^{-3}g/s)	r	p	GCI	$GCI_{asymptotic}$
Mesh 1	0.002	1.6521e-2				
Mesh 2	0.001	1.6478e-2	2	1.9668	0.11%	1.02
Mesh 3	0.0005	1.6467e-2	2		0.0287%	

The value of the convergence index is as small as 0.0287%. The ratio $GCI_{asymptotic}$ is close to 1, which shows that the solutions are within the asymptotic range. The total number of elements is 3,586,103 for Mesh 3.

The mass decline of the entire cylindrical gel sample is plotted in Figure 38. The predicted global evaporation rate by 3D simulation is close to the experimental result only for a short period, and significantly below the experiments (slower mass loss and gentle slope). This trend is similar to those for a hemispherical gel shown in Figure 37.

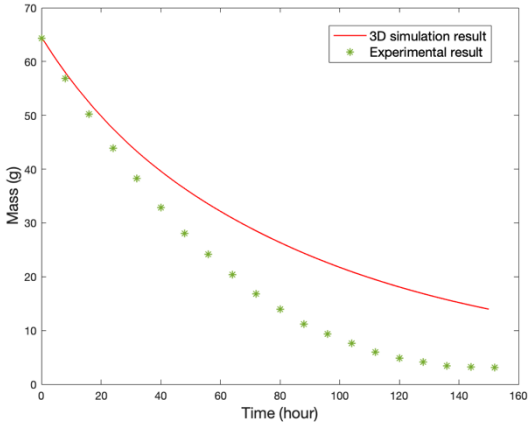

Fig. 39 The mass loss curve predicted by the 3D simulation model compared with the experimental result for the cylindrical gel sample

The main reasons for the large deviation at longer times are likely due to: (i) the assumption that the pores are in cylindrical shape and uniformly distributed in the gel; (ii) the surface porosity is assumed to be the same as the bulk porosity; (iii) convection in the air is ignored, which can significantly enhance the evaporation rate; (iv) the moving boundary at the surface of the gel is ignored. Another possible cause of the discrepancy for the cylindrical model is the neglect of the edge effect described in Section 7.2. In our simulation, the evaporation rate is uniform along the surface of the gel, which is not true based on the observation and analysis by Hu & Larson [95].

CHAPTER 8

CONCLUSION

The primary purpose of this study is to propose a CFD tool to predict the performance of the passive air freshener products from Henkel. As for the air freshener that absorbs fragrance by capillary force and evaporates with a wicking pad, the wicking behavior inside the fibrous porous material and the evaporation outside the wick have been studied. An experimental setup is performed to investigate the wicking and evaporation behavior. We employed numerical 2D simulation to study the wicking behavior inside the air freshener pad without evaporation. The simulation is performed using the commercial software COMSOL Multiphysics by coupling Darcy's law with the Phase Transport in Porous Media Interface module. The simulation results match the experimental results qualitatively. It is shown that our numerical method can be used to predict the wicking performance for different designs of the diffusion pad from Henkel company. It is also observed that the evaporation from the pad surface occurs simultaneously with the wicking process. The airflow model outside the diffusion pad extends the classical dynamic wicking model to the case with surface evaporation. The kinetic theory of evaporation at the air-liquid interface is coupled with dynamic wicking theory to predict the evaporation performance for a long period.

To simulate the complete performance history of the wick-based air freshener and compare it with the experiments, dimensionless 3D simulations using the commercial software COMSOL Multiphysics were performed with the air freshener placed in a chamber and in a lab room without a chamber. Taking the diffusion and buoyancy driven

natural convective effect into account, the simulation results for the wicking process by coupling the evaporation model with dynamic wicking matches the experimental results well. This also indicates the 2D effect on the wicking pad can be neglected when predicting the entire performance since the assumption that the pressure inside the wick is uniform at horizontal level in our study did not affect the accuracy. The simulation results match the experimental results well for both samples. This indicates our numerical model can be used to accurately predict the complete performance for any given design with different housing designs or in different environments. The numerical models allow us to evaluate the effects of various design parameters on the air freshener performance. These design parameters include the size of the bottle, the size of the wick, the wick microstructures, etc. In our simulation, temperature is a factor that contributes to the evaporation rate on the interface based on the kinetic theory. It is seen as constant both in the experiments and in the 3D simulations. The variation of temperature during evaporation was not taken into account in the analysis because the air freshener is generally used at room temperature without an extra heat source. Gatapova et al. [63] studied the temperature jump at water-air interface during evaporation and observed that the temperature jump and evaporation rate increase as the water is heated. At room temperature, the temperature jump at the interface is negligible. The temperature term in our evaporation model can still be adjusted based on the temperature in different regions or seasons. The effect of humidity was not considered either, which could be an important factor that influences the evaporation performance. It could be one of our future works.

A preliminary analysis is attempted on another product of Henkel, the gel-based air freshener. The experiments were performed with gel samples in two different shapes. To predict the evaporation performance of the gel in the shape of hemisphere, a sessile drop model developed by Hu & Larson [102] for the drying of a liquid droplet is employed. The sessile drop model can roughly predict the drying time for the gel. The evaporation model with kinetic theory is then applied as the boundary condition at the surface of the gel to predict the evaporation performance for the gel sample in the shape of hemisphere and cylinder. The analysis for the gel-based air freshener is more difficult than the wick-based air freshener due to the complex structure and unknown shape variation with the solid network of the gel. In our study, the porous network structure of the gel is constructed as cylindrical pores with the same radius connected with each other. As the liquid phase evaporates, the network shrinks with the number of the pores and the weight of the solid polymer maintains the same. The diffusion equation is solved, and the predicted change of total mass with time matches the experimental result qualitatively. These results further prove the validity of our method that couples the evaporation model of kinetic theory with diffusion equation to predict the evaporation performance from porous media. However, for both shapes of the gel samples, the deviation between the simulated results and experimental results increase with time. To better predict the evaporation performance of the gel, the convection effect in the surrounding air must be included in the simulation. The change of porosity and surface area also need to be addressed. The moving boundary of the gel surface also needs to be addressed. These issues can be addressed in future studies.

REFERENCES

[1] Mendez, Sergio; Fenton, Erin M.; Gallegos, Gil R.; Petsev, Dimiter N. etc, "Imbibition in Porous Membranes of Complex Shape: Quasi-stationary Flow in Thin Rectangular Segments," *Langmuir,* pp. 1380-1385, 2010.

[2] Fu, Elain; Ramsey,Stephen A.; Kauffman, Peter;Lutz, Barry; Yager, Paul, "Transport in two- dimensional paper networks," *Microfluid Nanofluid,* pp. 10:29-35, 2011.

[3] Martinez, A. W.; Phillips, W. T.; Whitesides; G. M., "Diagnostics for the Developing World: Microfluidic Paper-Based Analytical Devices.," *American Chemical Society,* pp. 3-10, 2010.

[4] Martinez, Andres W.; Phillips, Scott T.; Whitesides, George M., "Three-dimensional microfluidic devices fabricated in layered paper and tape," *PNAS,* vol. 105, no. 50, pp. 19606-19611, 2008.

[5] Fries, N.; Dreyer, M., "The effect of the evaporation on the wicking of liquids into a metallic weave," *Journal of Colloid and Interface Science,* vol. 321, pp. 118-129, 2008.

[6] Rogacs, A., Steinbrenner, J., Rowlette, J., Weisse, J., Zheng, X., & Goodson, K., "Characterization of the wettability of thin nanostructured films in the presence of evaporation.," *Journal of Colloid and Interface Science,* vol. 349, no. 1, p. 354–360, 2010.

[7] Weibel, J. A.; Garimella, S. V.; Murthy, J. Y.; Altman, D. H, "Design of Integrated Nanostructured Wicks for High-Performance Vapor Chambers," *IEEE Transactions on Components, Packaging and Manufacturing Technology,* vol. 1, no. 6, pp. 859-867, 2011.

[8] A. Steinemann, "Ten questions concerning air fresheners and indoor built environments," *Building and Environment,* vol. 111, pp. 279-184, 2017.

[9] R. Lucas, "Ueber das Zeitgesetz des kapillaren Aufstiegs von Flussigkeiten," *Kolloid-Zeitschrift,* no. 23, pp. 15-22, 1918.

[10] E. W. Washburn, "The dynamics of capillary flow," *Physics Review,* vol. 17, no. 3, p. 273, 1921.

[11] Siebold, A.; Nardin, M.; Schultz, J.; Walliser, A.; M. Oppliger., "Capillary Rise for Thermodynamic Characterrization of Solid Particle Surface.," *Journal of Colloid and Interface Science,* vol. 186, pp. 60-70, 1997.

[12] Siebold, Alain; Nardin, Michel; Schultz, Jacques; Walliser, Andre; Oppliger, Max, "Effect of dynamic contact angle on capillary rise phenomena," *Colloids and surfaces A: Physicochemical and engineering aspects ,* vol. 161, no. 1, pp. 81-87, 2000.

[13] T. Young, "III. An essay on the cohesion of fluids," *Philosophical transactions of the royal society of London ,* vol. 95, pp. 65-87, 1805.

[14] Bell, J. M; Cameron, F. K, "The Flow of Liquids through Capillary Spaces," *Journal of Physical Chemistry,* vol. 10, no. 8, pp. 658-674, 1952.

[15] Massodi, Reza; Pillai, Krishna M., "Darcy's Law-Based Model for Wicking in Paper-Like Swelling Porous Media," *AIChE Journal,* vol. 56, no. 9, pp. 2257-2267, 2010.

[16] D. Quéré, "Inertial capillarity," *EPL (Europhysics Letters),* vol. 39, no. 5, p. 533–538, 1997.

[17] A. A. Jeje, "Rates of Spontaneous Movement of Water in Capillary Tubes.," *Journal of colloid and interface science,* vol. 69, no. 3, p. 420–429, 1979.

[18] Petrash, D. A., Otto, E. W., Nelson, T. M., Effect of surface energy on the liquid-vapor interface configuration during weightlessness., National Aeronautics and Space Administration, 1963.

[19] R. Siegel, "Transient Capillary Rise in Reduced and Zero-Gravity Fields," *Journal of Applied Mechanics,* vol. 28, no. 2, p. 165–170, 1961.

[20] Joos, P.; Van Remoortere, P.; & Bracke, M., "The kinetics of wetting in a capillary," *Journal of Colloid and Interface Science,* vol. 136, no. 1, p. 189–197, 1990.

[21] Levine, S.; Reed, P.; Watson, E. J.; Neale, G., "A theory of the rate of rise of a liquid in a capillary," *Colloid and Interface Science,* vol. III, pp. 403-419, 1976.

[22] Zhmud, B. V.; Tiberg, F.; Hallstensson, K., "Dynamics of Capillary Rise," *Journal of Colloid and Interface Science,* vol. 228, pp. 263-269, 2000.

[23] Stange, Michael; Dreyer, Michael E.; Rath, Hans J., "Capillary driven flow in circular cylindrical tubes," *Physics of Fluids,* pp. 2587-2601, 2001.

[24] Dreyer, Michael; Delgado, Antonio; Rath, Hans-Joseph, "Capillary rise of liquid between parallel plates under microgravity," *Journal of Colloid and Interface Science,* vol. 163, pp. 158-168, 1994.

[25] H. Darcy, Darcy, Henry. Les fontaines publiques de la ville de Dijon: exposition et application..., Victor Dalmont, 1856.

[26] Masoodi, Reza; Pillai, Krishna M.; Varansi, Padma Prabodh, "Darcy's law-based models for liquid absorption in polymer wicks," *AIChE journal ,* vol. 53, no. 11, pp. 2769-2782, 2007.

[27] Jang, Ilhoon; Simon, Song, "Facile and precise flow control for a paper-based microfluidic device through varying paper permeability," *Lab on a Chip 15,* vol. 16, pp. 3405-3412, 2015.

[28] H. C. Brinkman, "A calculation of the viscous force exerted by a flowing fluid on a dense swarm of particles," *Flow, Turbulence and Combustion,* vol. 1, no. 1, pp. 27-34, 1949.

[29] Choi, J. R.; Liu, Z.; Hu, J.; Tang, R.; Gong, Y.; Feng, S.; Xu, F., "Polydimethylsiloxane-paper hybrid lateral flow assay for highly sensitive point-of-care nucleic acid testing.," *Analytical chemistry,* vol. 88, no. 12, pp. 6254-6264., 2016.

[30] Poudel, Sajag, An Zou, and Shalabh C. Maroo, "Wicking in cross-connected buried nanochannels.," *The Journal of Physical Chemistry C ,* vol. 123, no. 38, pp. 23529-23534, 2019.

[31] L. A. Richards, "Capillary conduction of liquids through porous mediums," *Physics ,* vol. 1, no. 5, pp. 318-333, 1931.

[32] Ashari, A., T. M. Bucher, H. Vahedi Tafreshi, M. A. Tahir, and M. S. A. Rahman, "Modeling fluid spread in thin fibrous sheets: Effects of fiber orientation," *International Journal of Heat and Mass Transfer ,* vol. 53, no. 9-10, pp. 1750-1758, 2010.

[33] Perez-Cruz, Angel; Stiharu, Ion; Dominguez-Gonzalez, Aurelio, "Two-dimensional model of imbibition into paper-based networks using Richards' equation," *Microfluid Nanofluid,* p. 21:98, 2017.

[34] Tirapu-Azpiroz, Jaione; Ademir Ferreira Silva, Matheus Esteves Ferreira, William Fernando Lopez Candela, Peter William Bryant, Ricardo Luis Ohta, Michael Engel, Mathias Bernhard Steiner, (2018), "Modeling fluid transport in two-dimensional paper networks," *Micro/Nanolith. MEMS ,* vol. 17(2), 2018.

[35] Barry, D., Parlange, J., Lockington, D., & Wissmeier, L. , "Comment on “The effect of evaporation on the wicking of liquids into a metallic weave” by N. Fries, K. Odic, M. Conrath and M. Dreyer.," *Journal of Colloid and Interface Science, ,* vol. 336, no. 1, p. 374–375, 2009.

[36] Jahanshahi-Anbuhi, S., Henry, A., Leung, V., Sicard, C., Pennings, K., Pelton, R., Brennan, J., & Filipe, C. , "Paper-based microfluidics with an erodible polymeric bridge giving controlled release and timed flow shutoff," *The Royal Society of Chemistry,* vol. 14, no. 1, pp. 229-236, 2013.

[37] Liu, Z; Hu, J; Zhao, Y; Qu, Z; Xu, F, "Experimental and Numerical Studies on Liquid Wicking into Filter Papers for Paper-based Diagnostics," *Applied Thermal Engineering,* vol. 88, pp. 280-287, 2015.

[38] R. a. A.-C. E. American Society of Heating, ANSI/ASHRAE Standard 62.1-2019 Ventilation for Acceptable Indoor Air Quality, New York: ANSI, 2019.

[39] Camplisson, C., Schilling, K., Pedrotti, W., Stone, H., & Martinez, A. , "Two-ply channels for faster wicking in paper-based microfluidic devices.," *Lab on a Chip,* vol. 15, no. 23, p. 4461–4466, 2015.

[40] Beyhaghi, S., Geoffroy, S., Prat, M., & Pillai, K., "Wicking and evaporation of liquids in porous wicks: A simple analytical approach to optimization of wick design.," *AIChE Journal,* vol. 60, no. 5, p. 1930–1940, 2014.

[41] Veran-Tissoires, S., Marcoux, M., & Prat, M., "Discrete salt crystallization at the surface of a porous medium.," *Physical review letters, ,* vol. 108, no. 5, p. 054502, 2012.

[42] Van Engeland, Charlotte, Benoît Haut, Laurent Spreutels, and Benjamin Sobac, "Evaporation versus imbibition in a porous medium," *Journal of colloid and interface science ,* vol. 576, pp. 280-290, 2020.

[43] Medina, A.;Perez-Rosales, C.; Pineda, A., "Imbibition in pieces of paper with different shapes," *Revista Mexicana De Fisica,* vol. 47, no. 6, pp. 537-541, 2001.

[44] Dharmaraja, S., Lafleur, L., Byrnes, S., Kauffman, P., Buser, J., Toley, B., ... & Lutz, B., "Programming paper networks for point of care diagnostics.," *In Microfluidics, BioMEMS, and medical microsystems XI,* vol. 861, p. 86150X, 2013.

[45] Toley, B., McKenzie, B., Liang, T., Buser, J., Yager, P., & Fu, E., "Tunable-Delay Shunts for Paper Microfluidic Devices.," *Analytical Chemistry (Washington),* vol. 85, no. 23, p. 11545–11552, 2013.

[46] Tang, R., Yang, H., Gong, Y., Liu, Z., Li, X., Wen, T., Qu, Z., Zhang, S., Mei, Q., & Xu, F. , "Improved Analytical Sensitivity of Lateral Flow Assay using Sponge for HBV Nucleic Acid Detection.," *Scientific Reports,* vol. 7, no. 1, pp. 1360-10, 2017.

[47] Ashari, A., and H. Vahedi Tafreshi, " A two-scale modeling of motion-induced fluid release from thin fibrous porous media," *Chemical Engineering Science,* vol. 64, no. 9, pp. 2067-2075, 2009.

[48] Ashari, A., and H. Vahedi Tafreshi, "General capillary pressure and relative permeability expressions for through-plane fluid transport in thin fibrous sheets.," *Colloids and Surfaces A: Physicochemical and Engineering Aspects ,* vol. 346, no. 1-3, pp. 114-122, 2009.

[49] Brooks, R. H. ; Corey, A. T., Hydraulic Properties of Porous Media, Hydrology Papers (Colorado State University), 1964.

[50] A. T. Corey, Mechanics of immiscible fluids in porous media, Highlands Ranch: Water Resources Publications, 1994.

[51] Lu, Xiang; Kharaghani, Abdolreza; Adloo, Hadi; Tsotsas, Evangelos, "The Brooks and Corey Capillary Pressure Model Revisited from Pore Network Simulations of Capillarity-Controlled Invasion Percolation Processes," *Processes,* vol. 8, no. 10, p. 1318, 2020.

[52] Chung, J.; Hulbert, G. M., "A time integration algorithm for structural dynamics with improved numerical dissipation: The generalized-alpha method," pp. 371-375, 1993.

[53] Aydar, Alev Y.; Rodriguez-Martinez, Veronica; Farkas, Brain E., "Determination and modeling of contact angle of Canola oil and olive oil on a PTFE surface at elevated temperatures using air or steam as surrounding media," *Food Science and Technology,* pp. 304-310, 2016.

[54] K. Galvin, A conceptually simple derivation of the Kelvin equation, vol. 60, Chemical Engineering Science, 2005, pp. 4659-4660.

[55] Metzger, T.; Tsotsas, E., "Influence of pore size distribution on drying kinetics: A simple capillary model," *Drying Technol.,* vol. 23, no. 9-11, pp. 1797-1809, 2005.

[56] Carey, V. P. , Liquid-Vapor Phase-Change Phenomenon, Taylor&Francis, 1992.

[57] Schrage, A Thermal Study of Interface Mass Transfer, New York: Columbia University Press, 1953.

[58] Simpson, H.C., Silver, R. S, Theory of one-dimensional, two-phase homogeneous non-equilibrium flow, Proceedings Institute of Mechanical Engineers Symposium on Two-phase Fluid Flow, 1962, pp. 45-53.

[59] Kucherov, R.Y., and Rikenglaz, L.E, The Problem of Measuring the Condensation Coefficient, vol. 133, Doklady Akad, 1960, pp. 1130-1131.

[60] P. Davidovits, D.R. Worsnop, J. T. Jayne, C. E. Kolb, "Mass accommodation coeffecient of water vapor on liquid water," *Geophysical Research Letters,* vol. 31, 2004.

[61] Mills, The Condensation of Steam at Low Pressures, Space Sciences Laboratory,University of California at Berkeley. , 1965.

[62] Badam, V. K.; Kumar, V.; Durst, F. ; Danov, K., "Experimental and theoretical investigations on interfacial temperature jumps during evaporation," *Therm. Fluid Sci.,* vol. 32, no. 1, pp. 276-292, 2007.

[63] Gatapova, Elizaveta Ya.; Irina A. Graur, Oleg A. Kabov ; Vladimir M. Aniskin d, Maxim A. Filipenko; Felix Sharipov; Lounès Tadrist, "The temperature jump at water-air interface during evaporation," *International Journal of Heat and Mass Transfer,* vol. 104, pp. 800-812, 2017.

[64] Faghri, A.; Zhang, Y., Transport Pheonomena in Multiphase Systems, Burlington: Elsevier, 2006.

[65] Joseph, Renardy, Fundamentals of Two Fluids Dynamics Part I and II (edited by F. John, et al)., 1992.

[66] S. Middleman, Modeling Axisymmetric Flows, San Diego: Academic Press, 1995.

[67] Shermon, Diffusion in solids, McGraw-Hill, 1963.

[68] Mathers, W. G.; Madden, A. J.; Piret, Edgar L., "Simultaneous heat and mass transfer in free convection," *Ind. Eng. Chem,* vol. 49, no. 6, pp. 961-968, 1957.

[69] Wagner, W; H. J. Kretzschmar, International Steam Tables-Properties of Water and Steam based on the Industrial Formulation IAPWS-IF97, Springer Vieweg, 2019.

[70] Y. A. Cengel and M. A. Boles, Thermodynamics, Mc Graw Hill, 2011.

[71] P. J. Roache, "Verification and Validation in Computational Science and Engineering," *Computing in Science Eng.,* vol. 1, pp. 8-9, 1998.

[72] L. Kwasniewski, "Application of Grid Convergence Index in FE Computation," *Bulletin of the Polish Academy of Sciences. Technical Sciences,* vol. 61, no. 1, pp. 123-128, 2013.

[73] S. B. L. K. A. K. John M. Behan, "Aqueous Perfume Oil Microemulsions". United State Patent 5,374,614, 20 Dec 1994.

[74] "Silica Aerogel," 2008. [Online]. Available: http://www.aerogel.org. [Accessed 2020].

[75] Brinker, C. Jerrrey; Scherer, George W., Sol-Gel: Science The physics and Chemistry of Sol-Gel Processing, Elsevier Science, 1990.

[76] T. K. Sherwood, "The Drying of Solids-I," *Industrial and Engineering Chemistry,* vol. 21, no. 1, pp. 12-16, 1929.

[77] Mosthaf, Klaus; Helmig, Rainer; Or, Dani, "Modeling and Analysis of Evaporation Processes from Porous Media on the REV scale," *Water Resour,* vol. 50, pp. 1059-1079, 2014.

[78] Lehmann, P., Assouline, S., & Or, D. , "Characteristic lengths affecting evaporative drying of porous media.," *Physical Review. E, Statistical, Nonlinear, and Soft Matter Physics,* vol. 77, no. 5 Pt 2, p. 056309–056309. , 2008.

[79] R. K. Dwivedi, "Drying behaviour of alumina gels," *Journal of Materials Science Letters,* vol. 5, no. 4, pp. 373-376, 1986.

[80] Wayner, P. C ; Jr.; Kao, Y. K; LaCroix L. V., "The Interline Heat-transfer Coefficient of an Evaporating Wetting Film," *Int. J. Heat Mass Transfer,* vol. 19, pp. 487-492, 1976.

[81] H. H. Macey, "Clay-water relationships and the internal mechanism of drying.," *Trans. Br. Ceram. Soc,* vol. 41, pp. 73-121, 1942.

[82] J. J. Spitzer, "Electrostatic calculations on swelling pressures of clay-water dispersions.," *Langmuir,* vol. 5, no. 1, pp. 199-205, 1989.

[83] E. U. Schlünder, "On the Mechanism of the Constant Drying Rate Period and Its Relevance to Diffusion Controlled Catalytic Gas Phase Reactions," *Cheminal Engineering Science,* vol. 43, no. 10, pp. 2685-2688, 1988.

[84] Haghighi, E.; Shahraeeni, E.; Lehmann, P.; Or, D., "Evaporation rates across a convective air boundary layer are dominated by diffusion," *Water Resources Research,* vol. 49, pp. 1602-1610, 2013.

[85] E. U. Schlünder, "Drying of Porous Material During the Constant and the Falling Rate Period: A Critical Review of Existing Hypotheses," *Drying Technol.,* vol. 22, pp. 1517-1532, 2004.

[86] Talbi, Marouane; Prat, Marc, "About Schlünder's model: A Numerical Study of Evaporation from Partially Wet Surface," *Drying Technology, Taylor & Francis,* vol. 37, pp. 513-524, 2018.

[87] Laurindo, Joao Borges; Prat, Marc, "Numerical and Experimental Network Study of Evaporation in Capillary Porous Media. Phase Distributions," *Chemical Engineering Science,* vol. 51, no. 23, pp. 5171-5185, 1996.

[88] Laurindo, Joao Borges; Prat, Marc, "Numerical and experimental network study of evaporation in Capillary Porous Media," *Chemical Engineering Science,* vol. 53, no. 12, pp. 2257-2269, 1998.

[89] Stauffer, D.; Aharaony, A., Introduction to Percolation Theory, London: Taylor & Francis, 1992.

[90] M. Prat, "Recent advances in Pore-scale models for drying of porous media," *Chemical Engineering Journal,* vol. 86, pp. 153-164, 2002.

[91] Yiotis, Andreas G. ;Tsimpanogiannis, Ioannis N. ; Stubos, Athanassios K.; Yortsos, Yannis C., "Pore-network Study of the Characteristic Periods in the Drying of

Porous Materials," *Journal of Colloid and Interface Science,* vol. 297, pp. 738-748, 2006.

[92] Shokri, N.; Lehmann, P.; Or, D., "Chracteristics of Evaporation from Partially Wettable Porous Media," *Water Resources Research,* vol. 45, p. W02415, 2009.

[93] Shokri, N.; Lehmann, P.; Or, D., "Effects of Hydrophobic Layers on Evaporation from Porous Media," *Geophysical Research Letters,* vol. 35, p. L19407, 2008.

[94] T. R. Mikkelsen and R. F. Theiler, "Water-Based Gel With Low Syneresis". United State Patent US 2013/0157922 A1, 20 June 2013.

[95] H. Hu and R. G. Larson, "Analysis of the Effects of Marangoni Stresses on the Microflow in an Evaporating Sessile Droplet," *Langmuir,* vol. 21, pp. 3972-3980, 2005.

[96] Birdi, K. S.; Vu, D. T. ; Winter, A., "A study of the evaporation rates of small water drops placed on a solid surface.," *The Journal of physical chemistry,* vol. 93, no. 9, pp. 3702-3703, 1989.

[97] Shanahan, M. E. R; Bourges, C, "Effects of evaporation on contact angles on polymer surfaces," *Int. J. Adhesion and Adhesives,* vol. 14, no. 3, pp. 201-205, 1994.

[98] Bourges-Monnier, C., & Shanahan, M. E. R. , " Influence of evaporation on contact angle," *Langmuir,* vol. 11, no. 7, pp. 2820-2829, 1995.

[99] Rowan, S. M.; McHale, G.; Newton, M. I. J., "Evaporation of microdroplets and the wetting of solid surfaces," *J. Phys. Chem.,* vol. 11, p. 2820, 1995.

[100] Erbil. H. Y.; Meric, R. A., "Evaporation of Sessile Drops on Polymer Surfaces: Ellipsoidal Cap Geometry," *J. Phys. Chem,* vol. 101, no. 35, pp. 6867-6873, 1997.

[101] Meric, R. A.; Erbil, H. Y., "Evaporation of sessile drops on solid surfaces: Pseudospherical cap geometry," *Langmuir,* vol. 14, no. 7, pp. 1915-1920, 1998.

[102] Hu, Hua; Larson, R. G., "Evaporation of a sessile droplet on a substrate," *J. Phys. Chem,* vol. 106, pp. 1334-1344, 2002.

[103] N. N. Lebedev, Special functions and their applications, Englewood Cliffs, New Jersey: Prentice-Hall, 1965.

[104] Mathias Dunkel, Ulrike Schmidt, Swantje Struck, Lena Berger, Bjoern Gruening, Julia Hossbach, Ines S. Jaeger, Uta Effmert, Birgit Piechulla, Roger Eriksson, Jette

Knudsen, Robert Preissner, " SuperScent—a database of flavors and scents," *Nucleic Acids Research,* vol. 37, no. 1,1, pp. D291-D294, 2009.

[105] Stein. D. J.; Maskara, A.; Haereid, S.; Anderson, J.; Smith, D.M., "Contact angle measurement and its application to Sol-gel processing," *Materials Research Society,* vol. 346, pp. 643-648, 1994.

[106] Sharma, Archana; Bhat, Sumrita; Vishnoi, Tanushree; Nayak, Vijayashree; Kumar,Ashok, "Three-Dimensional Supermacroporous Carrageenan-Gelatin Cryogel Matrix for Tissue Engineering Applications," *BioMed Research International,* vol. 2013, 2013.

[107] Wallace, Stephen; Hench, Larry L., "Structural Analysis of Water Adsorbed in Silica Gel," *Journal of Sol-Gel Science and Technology,* vol. 1, pp. 153-168, 1994.